Monthly Notices
of the
ROYAL ASTRONOMICAL SOCIETY

Mon. Not. R. Astron. Soc. **405,** 759–776 (2010) doi:10.1111/j.1365-2966.2010.16499.x

The JCMT Legacy Survey of the Gould Belt: a first look at Taurus with HARP

C. J. Davis,[1⋆] A. Chrysostomou,[1] J. Hatchell,[2] J. G. A. Wouterloot,[1] J. V. Buckle,[3,4] D. Nutter,[5] M. Fich,[6] C. Brunt,[2] H. Butner,[7] B. Cavanagh,[1] E. I. Curtis,[3,4] A. Duarte-Cabral,[8] J. Di Francesco,[9,10] M. Etxaluze,[11,12] P. Friberg,[1] R. Friesen,[9,10] G. A. Fuller,[8] S. Graves,[3,4] J. S. Greaves,[13] M. R. Hogerheijde,[14] D. Johnstone,[9,10] B. Matthews,[9] H. Matthews,[9,15] J. M. C. Rawlings,[16] J. S. Richer,[3,4] J. Roberts,[17] S. Sadavoy,[9,10] R. J. Simpson,[5] N. Tothill,[2] Y. Tsamis,[18] S. Viti,[16] D. Ward-Thompson,[5] Glenn J. White,[11,12] and J. Yates[16]

[1]*Joint Astronomy Centre, 660 North A'ohōkū Place, University Park, Hilo, HI 96720, USA*
[2]*School of Physics, University of Exeter, Stocker Road, Exeter EX4 4QL*
[3]*Cavendish Laboratory, Cambridge University, J. J. Thomson Avenue, Cambridge CB3 9HE*
[4]*Kavli Institute for Cosmology, c/o Institute of Astronomy, University of Cambridge, Madingley Road, Cambridge CB3 0HA*
[5]*School of Physics and Astronomy, Cardiff University, 5 The Parade, Cardiff CF24 3AA*
[6]*Department of Physics and Astronomy, University of Waterloo, Waterloo, Ontario, Canada*
[7]*Department of Physics and Asrtronomy, James Madison University, 901 Carrier Dr., Harrisonburg, VA 22807, USA*
[8]*Jodrell Bank Centre for Astrophysics, School of Physics and Astronomy, Alan Turing Building, The University of Manchester, Manchester M13 9PL*
[9]*Herzberg Institute of Astrophysics, National Research Council of Canada, 5071 W. Saanich Rd., Victoria, BC, Canada*
[10]*Department of Physics and Astronomy, University of Victoria, 3800 Finnerty Road, Victoria, BC, Canada*
[11]*Department of Physics and Astronomy, Open University, Walton Hall, Milton Keynes MK7 6AA*
[12]*Science and Technology Facilities Council, Rutherford Appleton Laboratory, Chilton, Didcot OX11 0QX*
[13]*Scottish Universities Physics Alliance, Physics and Astronomy, University of St. Andrews, North Haugh, St. Andrews KY16 9SS*
[14]*Leiden Observatory, Leiden University, PO Box 9513, 2300 RA, Leiden, the Netherlands*
[15]*Dominion Radio Astrophysical Observatory, National Research Council of Canada, White Lake Road, Penticton, Canada*
[16]*Department of Physics and Astronomy, University College London, Gower Street, London*
[17]*Centro de Astrobiologia (CSIC/INTA), Instituto Nacional de Tecnica Aeroespacial, Ctra. de Torrejon a Ajalvir km 4, E-28850 Torrejon de Ardoz, Madrid, Spain*
[18]*Instituto de Astrofísica de Andalucía (CSIC), Camino Bajo de Huétor 50, 18008 Granada, Spain*

Accepted 2010 February 9. Received 2010 January 28; in original form 2009 December 1

ABSTRACT

As part of a James Clerk Maxwell Telescope (JCMT) Legacy Survey of star formation in the Gould Belt, we present early science results for Taurus. CO $J = 3$–2 maps have been secured along the north-west ridge and bowl, collectively known as L 1495, along with deep ^{13}CO and C^{18}O $J = 3$–2 maps in two subregions. With these data, we search for molecular outflows, and use the distribution of flows, Herbig–Haro (HH) objects and shocked H_2 line-emission features, together with the population of young stars, protostellar cores and starless condensations to map star formation across this extensive region. In total, 21 outflows are identified. It is clear that the bowl is more evolved than the ridge, harbouring a greater population of T Tauri stars and a more diffuse, more turbulent ambient medium. By comparison, the ridge contains a much younger, less widely distributed population of protostars which, in turn, is associated with a greater number of molecular outflows. We estimate the ratio of the numbers of pre-stellar to protostellar cores in L 1495 to be ∼1.3–2.3, and of gravitationally unbound starless cores to (gravitationally bound) pre-stellar cores to be ∼1. If we take previous estimates

⋆E-mail: cjd@jach.hawaii.edu

of the protostellar lifetime of $\sim 5 \times 10^5$ yr, this indicates a pre-stellar lifetime of $9(\pm 3) \times 10^5$ yr. From the number of outflows, we also crudely estimate the star formation efficiency in L 1495, finding it to be compatible with a canonical value of 10–15 per cent. We note that molecular outflow-driving sources have redder near-infrared colours than their HH jet-driving counterparts. We also find that the smaller, denser cores are associated with the more massive outflows, as one might expect if mass build-up in the flow increases with the collapse and contraction of the protostellar envelope.

Key words: stars: formation – ISM: individual: Taurus – ISM: jets and outflows – ISM: kinematics and dynamics.

1 INTRODUCTION

The Gould Belt Survey (GBS; Ward-Thompson et al. 2007a) is a large, legacy programme currently underway at the James Clerk Maxwell Telescope (JCMT). The goal is to gather both heterodyne line observations and submillimetre (submm) continuum images of nearby star-forming regions. The survey targets the Gould Belt, which is a ring of O-type stars and molecular clouds with a radius of $\sim$350 pc. It is inclined at $\sim 20^\circ$ to the Galactic plane and is centred on a point 200 pc from the Sun (ascending node, $\Omega = 275$–295; Torra, Fernández & Figueras 2000). The Gould Belt includes well-known regions such as Orion, Taurus-Auriga-Perseus, Serpens, Lupus, Ophiuchus and the Pipe nebula. Taurus is one of four regions initially targeted in ^{12}CO $J = 3$–2 (hereafter CO 3–2), ^{13}CO 3–2 and C^{18}O 3–2. These four regions – Orion A (Buckle et al. 2010), Serpens (Graves et al. 2010), Ophiuchus (White et al., in prep.) and Taurus (this paper) – were selected as being complementary, active, nearby, relatively well-known and well studied. Extensive submm continuum mapping, at 450 and 850 μm, is also planned as part of the survey (Ward-Thompson et al. 2007a).

In studies of nearby, low-mass star-forming regions CO 3–2 emission samples the denser, warmer gas which often envelopes cores where new stars are forming (temperatures $\sim 10 - 50$ K; gas densities of the order of 10^4–10^5 cm^{-3}). CO 3–2 is also a proven tracer of outflow activity (e.g. Hatchell, Fuller & Ladd 1999; Davis et al. 2000a; Knee & Sandell 2000; Bussmann et al. 2007; Hatchell, Fuller & Richer 2007a; Lee et al. 2007; Yeh et al. 2008). With the JCMT, moderate spatial resolution is attainable at 345 GHz ($\sim$14 arcsec), which often allows one to disentangle multiple outflows in clustered regions. The higher critical density for excitation of the 3–2 line (over, say, the 1–0 emission line) can also lead to better maps of the dense, more collimated flow components. Molecular outflows are known to emanate from the very youngest sources, objects that are still accreting most of their final mass. New, large-scale surveys in CO can therefore be used to identify the locations of these embedded protostars, leading to a more complete census of the youngest stars, and an indication of the overall youth and star formation activity in a region (e.g. Hatchell et al. 2007a; Davis et al. 2008; Hatchell & Dunham 2009; Buckle et al. 2010).

Taurus is a much-studied region of low-mass star formation (see Kenyon, Gómez & Whitney 2009, for a detailed review). The Taurus molecular cloud covers an area in excess of 100 deg^2 (Ungerechts & Thaddeus 1987; Goldsmith et al. 2008; Narayanan et al. 2008). LDN 1495 (L 1495 hereafter) is one of three main areas associated with a high density of young stars. L 1495 lies in the NW corner of Taurus and coincides with Barnard dark nebulae B 7, 10, 209, 211, 213 and 216. In molecular line and extinction maps L 1495 comprises an extended, knotty filament – here referred to as the 'SE ridge' – and, at its northern extremity, a more diffuse cloud – the 'bowl'. Goldsmith et al. (2008) refer to the ridge as B 231 and label only the bowl L 1495. From their extensive CO observations, they estimate masses of 1095 and 2626 $M_\odot$ for the ridge and bowl, respectively, and assign areas of 13.7 pc^2 (2.3 deg^2) and 31.7 pc^2 (5.3 deg^2) for each region (see their Table 4). They also note that, quite remarkably, the SE ridge is 75 arcmin (3 pc) long yet only 4.5 arcmin (0.2 pc) wide. A similar collimated feature in the NGC 6334 star-forming region has recently been analysed by Matthews et al. (2008).

In this paper, we split the bowl into four areas, L 1495 N, S, E and W, and label the ridge L 1495 SE. L 1495 E harbours the classical T Tauri star (TTS) CoKu Tau-1 and HH 156 (Eislöffel & Mundt 1998); L 1495 W (B 209) is associated with the TTS CW Tau (Elias 1, Hubble 4) which drives HH 220 and possibly also HH 826-828 (Gómez de Castro 1993; McGroarty & Ray 2004). HH 390/391/392 and HH 157 are located along the L 1495 SE ridge (Gomez, Whitney & Kenyon 1997; Eislöffel & Mundt 1998); HH 157 is driven by the TTS Haro 6-5B (FS Tau B) and comprises a spectacular Herbig–Haro (HH) jet and bow shock that extend over 30–40 arcsec.

L 1495 W has been mapped in C^{17}O 1–0, C^{18}O 1–0, CS 2–1, N_2H^+ 1–0 (at the Five College Radio Astronomy Observatory (FCRAO)) and in NH_3 (1,1) and (2,2) emission (at Effelsberg) by Tafalla et al. (2002) – the region they label 'L 1495' roughly coincides with L 1495 W. N_2H^+ 1–0 maps of the SE ridge are presented by Tatematsu et al. (2004). More extensive ^{13}CO and C^{18}O 1–0 maps of Taurus are discussed by Mizuno et al. (1995) and Onishi et al. (1996); CO and ^{13}CO 1–0 maps, covering 98 deg^2 with 45 arcsec resolution, have recently been published by Narayanan et al. (2008) and Goldsmith et al. (2008). Finally, extensive yet high spatial resolution H^{13}CO$^+$ 1–0 observations of the molecular cores in Taurus, including the L 1495 ridge and bowl, are discussed by Onishi et al. (2002, hereafter OMK02). These H^{13}CO$^+$ observations, to which we refer throughout the paper, were obtained at the 45-m Nobeyama telescope with a beam width of 20 arcsec.

Kenyon & Hartmann (1995) present a list of $\sim$300 young stellar objects (YSOs) in Taurus, derived from multiwavelength observations and complemented recently with data from the *Spitzer Space Telescope* (Hartmann et al. 2005; Luhman et al. 2006, though note that the *Spitzer* observations do not cover L 1495 W or the bottom of the SE ridge). Many of the youngest sources have been observed in the 1.3-mm continuum survey obtained by Motte & André (2001). In L 1495, the young stars are clustered towards the eastern and western sides of the L 1495 bowl, and are tightly bound along the narrow, SE ridge. The protostellar population as a whole is discussed in the review of Kenyon et al. (2009), who also present an updated list of YSOs in Taurus. Kenyon et al. note in their article that classical TTSs typically have near-infrared (near-IR) colours $H - K_s < 1 - 1.5$ and mid-IR colours [3.6]–[4.5] $\sim$ 0.5–1.0 and

[5.8]–[8.0] ∼ 0.25–0.75; embedded protostars (Class 0/I sources) are expected to be redder.

In this paper, we use an up-to-date list of 'Taurus Young Stars', kindly provided by K. Luhmann, to search for candidate outflow sources in L 1495. This list is essentially the same as that presented by Kenyon et al. (2009). We also assume that 'starless' cores are low-mass ($M < 10$ $M_{\odot}$) dense cores without compact luminous sources of any mass (Di Francesco et al. 2007). 'Pre-stellar' cores are a subset of starless cores, since they must also be gravitationally bound (Ward-Thompson et al. 2007b). Establishing whether a core is bound or not is observationally very difficult (although the virial theorem gives some indication). We therefore refer to cores that are not obviously associated with a young star as starless; cores that do appear to contain a young star are referred to as 'protostellar'.

Traditionally, a distance of 140 pc has been used for Taurus (Elias 1978; Ungerechts & Thaddeus 1987), on the basis of estimates from star counts (McCuskey 1939), the reddening of field stars as a function of distance (Gottlieb & Upson 1969) and photometric distances measured to the exciting stars of reflection nebulae (Racine 1968). Analysis of the velocity field in wide-field molecular line studies suggests that ambient gas velocities change by only a few km s^{-1} across Taurus, and are particularly limited across L 1495 (Ungerechts & Thaddeus 1987; Goldsmith et al. 2008; Narayanan et al. 2008, see also Section 3.1 below). This supports a more-or-less common distance to the molecular clouds and star-forming regions in Taurus. Recent trigonometric parallax measurements suggest that the eastern portion of Taurus may be farthest from us, at a distance of ∼161 pc, with the south (around T Tau) at an intermediate distance of 147 pc and the west, L 1495, marking the near side of the cloud at a distance of 130 pc (Torres et al. 2009). However, these distances are based on parallax measurements for only a handful of stars. We therefore adopt the canonical distance of 140 pc for L 1495, consistent with previous studies, most notably Goldsmith et al. (2008) and OMK02.

Overall, our goal with this paper is to search for outflows in L 1495, identify their driving sources, and compare the properties of these outflows with those of the driving sources and associated molecular cores.

2 OBSERVATIONS AND DATA REDUCTION

2.1 Data acquisition

As part of the JCMT Gould Belt Legacy Survey, the 325–375 GHz Heterodyne Array Receiver Programme (HARP) was used to map 18 near-contiguous regions across the L 1495 bowl and along the SE ridge in CO 3–2 emission (Fig. 1 and Table 1), as well as two smaller subregions in ^{13}CO 3–2 and C^{18}O 3–2 emission. The Heterodyne Array Receiver Programme (HARP) is a 16 receptor (4 × 4 array) single side-band superconductor-insulator-superconductor (SIS) receiver system acting as a front-end to the Auto-Correlation Spectral Imaging System (ACSIS) (Hovey et al. 2000; Smith et al. 2003; Buckle et al. 2009).

CO 3–2 data at a rest frequency of 345.79599 GHz were acquired in dual subband mode. Maps with modest and high spectral resolution were acquired simultaneously, with 1024 ACSIS channels covering a bandwidth of 1.0 GHz at a spectral resolution of 977 kHz (0.85 km s^{-1}), and with 4096 channels covering a bandwidth of 250 MHz at a spectral resolution of 61 kHz (0.05 km s^{-1}). Only the latter are presented in this paper. In separate observations, ^{13}CO 3–2 (330.58796 GHz) and C^{18}O 3–2 (329.33055 GHz) data were acquired simultaneously in dual subband mode using only the high spectral resolution set-up. At these frequencies, the telescope Half Power Beam Width measures 14 arcsec, corresponding to 0.0095 pc at a distance of 140 pc.

Maps were obtained by scanning the telescope along rows parallel to the sides of the pre-defined mapping areas, each row separated

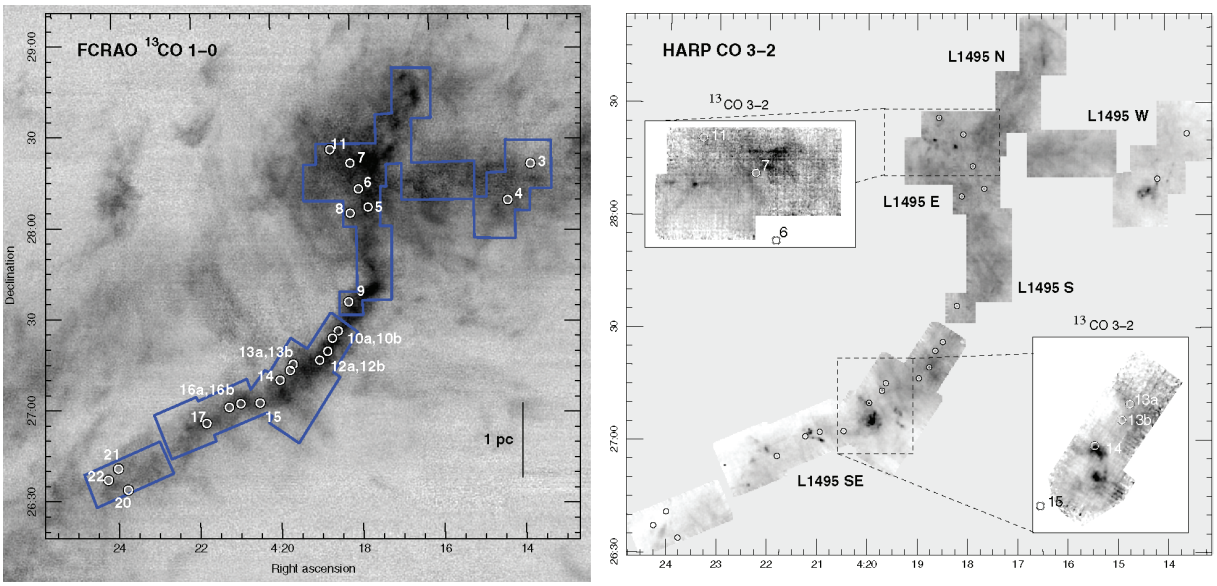

Figure 1. Left-hand panel: an overview of L 1495 in the north-west (NW) corner of Taurus. The image shows integrated ^{13}CO 1–0 emission from the FCRAO survey of Goldsmith et al. (2008). The positions of the H^{13}CO$^+$ cores identified by OMK02 are marked with circles and labelled using their core numbering scheme. Right-hand panel: a complete map of all regions observed with HARP in CO 3–2 (intensity integrated between 2.0 and 11.0 km s^{-1}), with the positions of the H^{13}CO$^+$ cores again marked. The areas mapped in ^{13}CO and C^{18}O 3–2 are also indicated; maps of ^{13}CO emission, integrated between 4.9 and 9.1 km s^{-1}(L 1495 E) and 4.5 and 8.2 km s^{-1}(L 1495 SE), are shown inset as grey-scale images. In the main text, we refer to L 1495 N, E, S and W as the bowl, and L 1495 SE as the south-east (SE) ridge.

Table 1. Log of CO 3–2 observations in L 1495.

Region[a]	Area[a]	Cube[a]	Date[a] (yyyy-mm-dd)	RA[b] (J2000.0)	Dec.[b] (J2000.0)	PA[c] (°)	Map size[c] (arcmin^2)	v_o [d] (km s^{-1})
Bowl	L 1495 E	L 1495	2007-11-24	4:18:04.8	28:21:45	90	20 × 10	6.6–7.1
	L 1495 E	L 1495-S	2007-12-22	4:17:50.0	28:09:00	0	10 × 15	5.9–6.7
	L 1495 E	L 1495-S2	2008-09-17	4:18:48.0	28:14:30	0	10 × 10	∼5.9–6.7
	L 1495 N	L 1495-NE1	2008-11-08	4:16:59.0	28:30:13	0	10 × 14	∼6.7
	L 1495 N	L 1495-NE2	2009-01-30	4:16:28.1	28:45:33	0	10 × 14	∼6.7
	L 1495 S	L 1495-S3	2008-11-08	4:17:34.0	27:49:20	0	10 × 22	6.6–6.8
	L 1495 S	L 1495-SE1	2008-03-29	4:18:09.1	27:35:17	0	5 × 5	5.6
	L 1495 W	L 1495-W	2008-08-21	4:14:10.0	28:12:00	0	10 × 10	6.7
	L 1495 W	L 1495-W1	2009-01-31	4:15:54.7	28:16:33	0	22 × 10	∼6.7
	L 1495 W	L 1495-W2	2008-10-07	4:14:34.0	28:04:00	0	13 × 13	6.7
	L 1495 W	L 1495-W3	2009-01-30	4:13:35.0	28:22:13	0	13 × 13	6.7
Ridge	L 1495 SE	L 1495-SE2	2008-03-15	4:18:41.3	27:22:00	147	8 × 15	5.3–5.7
	L 1495 SE	L 1495-SE3	2007-11-25	4:19:42.4	27:13:24	147	8 × 15	6.5
	L 1495 SE	L 1495-SE3b	2008-01-12	4:20:10.0	27:05:00	147	10 × 10	6.4
	L 1495 SE	L 1495-SE3c	2008-09-17	4:19:22.0	27:04:06	147	9 × 23	∼6.4
	L 1495 SE	L 1495-SE4	2008-08-21	4:21:14.1	27:01:11	113	10 × 20	6.6–6.7
	L 1495 SE	L 1495-SE4b	2008-10-07	4:22:22.0	26:55:00	113	10 × 10	∼6.6
	L 1495 SE	L 1495-SE5	2008-11-08	4:23:44.5	26:39:00	113	9 × 25	6.6–6.7

[a]The areas in the bowl and ridge regions of L 1495 are made up of multiple data cubes, often observed on different nights.
[b]Coordinates of the cube centres.
[c]Cube map size and position angle of the map long axis (measured E of N); with 'basket-weave' mapping the scan direction is along and orthogonal to this axis.
[d]The local standard of rest (LSR) velocities of the $H^{13}CO^+$ cores found in or near (if an approximate value is given) each region by OMK02, which we adopt as the local ambient gas velocity.

by half or a quarter of an array to improve the spatial sampling. This map is then repeated but by scanning in a perpendicular direction. This strategy of 'basket weaving' helps to generate flatter maps and evens out the noise in the final data cube. For most of the data presented here, two to four receptors were inoperable; for those fields where four receptors were unavailable (regions S2, W2, SE3c and SE4b), the array was stepped by a quarter of the array to prevent empty spaces or poorly sampled regions in the final maps.

Depending on map size, the ^{12}CO data cubes were obtained by integrating for 0.6 or 1.2 s (the 'sample time') for each 7.3 arcsec pixel on the sky. A reference position (usually observed at the end of each row in a scan), located at $4^h12^m24.9^s$ (J2000.0) 26°50′39″, was used throughout. A sample time of 1.0 s was used with the smaller ^{13}CO/C^{18}O maps.

The CO 3–2 data were observed in grade 3 weather [τ(225 GHz) ∼0.08–0.12]; better weather [τ(225 GHz) ∼0.05–0.065] was used for the ^{13}CO 3–2 and C^{18}O 3–2 data. System temperatures for the ^{12}CO data ranged from 340 to 580 K (<450 K in most regions); for the isotopologues temperatures were typically 300–500 K.

The regions mapped in ^{12}CO are listed in Table 1; these were defined based on large-scale extinction maps (Dobashi et al. 2005), the surveys of dense cores conducted by OMK02, and the locations of HH objects. Only regions with bright ^{12}CO emission were mapped in ^{13}CO and C^{18}O: two overlapping maps centred near $H^{13}CO^+$ cores 6, 7 and 11 were repeated a number of times to reduce the noise in the final cube; the full map covers an area of ∼22 × 12 arcmin^2, although note that the noise is roughly a factor of 2 higher in the north and west portion (∼60 per cent) of the map. Similarly, two overlapping maps covering cores 13a, 13b and 14 were repeated in the L 1495 SE ridge; in this case, the map covers a rectangular area of approximately 20 × 6 arcmin^2, though again the NW quarter of the map is about three-times noisier than the rest of the data cube. In all, 11 overlapping maps were co-added in L 1495 E, and 11 in L 1495 SE. The regions covered in ^{13}CO and C^{18}O are marked in Fig. 1.

2.2 Data processing

The individual CO 3–2 data cubes listed in Table 1 (third column) were reduced using the automated ORAC-DR pipeline (Cavanagh et al. 2008). Bad or overly noisy spectra were identified by the pipeline, based on quality assurance criteria[1] stipulated for the GBS legacy data, and these were first removed and noisy regions at the band edges trimmed. The resulting time-series data were regridded to a three-dimensional data cube and regions of line emission identified and masked out. A fifth-order polynomial was fit to the resulting emission-free regions and subtracted from each reduced cube. Cubes observed at the same spatial and spectral position were combined and a new baseline region mask was determined from this higher signal-to-noise ratio cube. This was applied to the individual cubes, which were then mosaicked and co-added together using a light Gaussian smoothing kernel with a Full Width Half Maximum (FWHM) ∼7.3 arcsec, to produce the final cubes and images. The inverse of this baseline mask identifies the line-emission regions and this was used to determine the integrated intensity and velocity images presented in this paper. Note that the Gaussian smoothing results in a spatial resolution to point sources of about 16 arcsec.

Special care was taken to remove striping from the data cubes when present (Curtis, Richer & Buckle 2010). This was done by determining the receptor-to-receptor response for the whole time-series, and dividing that response out. This technique does assume

[1]Receiver system temperature >600 K, noise across the spectrum exceeds 50 per cent of the mean noise level in all spectra, or spectrum baseline deviates by more than 10 per cent from the mean.

a priori that each receptor is exposed to similar emission during the scan. Given the diffuse and extended nature of the CO emission from Taurus, this technique worked well in eliminating or, at the very least, in minimizing the striping.

In CO 3–2, the noise is relatively uniform across the extensive region mapped. In the unbinned data (at the full 0.05 km s^{-1} resolution), at velocities within a few km s^{-1} of the ambient, the rms noise level [T_A^*(rms)] measures 0.10–0.20 K in L 1495 E, N and S (being highest in the south), 0.08–0.15 K in L 1495-W (highest in the NW), and 0.08–0.16 K along the SE ridge (it is a little higher, ∼0.22 K, in the data around cores 10, 10b and 12a).

The ^{13}CO and C^{18}O data were reduced in the same way. As noted above, the maps in ^{13}CO and C^{18}O were repeated a number of times. We found that in order to produce the optimal co-added map, the worst quality data had to be discarded before being included in the map reconstruction. This was done by measuring the rms of each of the spectra in the input data and masking those with the highest rms before generating the map. An iterative method was used to determine the optimal rms value to apply as a mask. In each step of the iteration, the data were masked using a different limiting rms before being reconstructed into a map using the Starlink MAKECUBE routine (Jenness et al. 2008). The rms in the reconstructed map was then measured. The limiting rms was varied to produce a reconstructed map with the lowest rms. This map was taken to be the optimal map. In the final, co-added maps the rms noise level measures T_A^*(rms) ∼ 0.13–0.20 K in ^{13}CO and ∼0.16–0.25 K in C^{18}O at the unbinned spectral resolution of 0.05 km s^{-1}. As mentioned earlier, the noise level is somewhat higher in the NW regions of each map.

In this article, all images are presented in units of antenna temperature (T_A^*). When calculating outflow parameters, integrated antenna temperature has been converted to main beam brightness temperature, $T_b = T_A^*/(\eta_{mb})$, using an aperture efficiency $\eta_{mb} = 0.63$ (Buckle et al. 2009).

3 RESULTS

3.1 Overall distribution of CO 3–2 emission and large-scale velocity structure

The entire region mapped in CO 3–2 with HARP is shown in Fig. 1, where we also show integrated ^{13}CO 3–2 images of the L 1495 E and L 1495 SE regions observed in this isotopologue (and in C^{18}O – data not shown). For comparison purposes, we also present the ^{13}CO 1–0 map of Goldsmith et al. (2008).

When mapping L 1495 in CO 3–2, we followed the high-extinction ridge of dense cores observed in C^{18}O 1–0 and H^{13}CO$^+$ 1–0 by Onishi et al. (1996) and OMK02, respectively; the ridge is evident in the ^{13}CO 1–0 integrated intensity map reproduced in Fig. 1. In L 1495, the CO 3–2 emission is generally faint, diffuse and/or optically thick: the integrated antenna temperature is <10.0 K ms^{-1} over 99 per cent of the mapped region, while we estimate the ^{12}CO opacity, τ_{12}, to be in the range of 3–38 in regions where ^{13}CO has been observed (although values will be overestimated where profiles are self-absorbed – see Section 3.2 for details). There are a number of compact knots superimposed on this diffuse emission, most of which are associated with outflows rather than cores. Indeed, the CO 3–2 emission features are by and large unrelated to the compact cores identified in H^{13}CO$^+$. Unfortunately, there is very little submm continuum data in L 1495 for comparison purposes (in their pointed 1.3-mm survey of young stars, Motte & André (2001) observe only nine sources in L 1495); only observations of cores 13a, 13b and 14 were found in the Submillimetre Common User Bolometer Array (SCUBA) Legacy Catalogue (Di Francesco et al. 2008) and only the dense cores themselves were detected. However, the entire area will be mapped at 450 and 850 μm with SCUBA-2 (Holland et al. 2006) as part of the GBS (Ward-Thompson et al. 2007a).

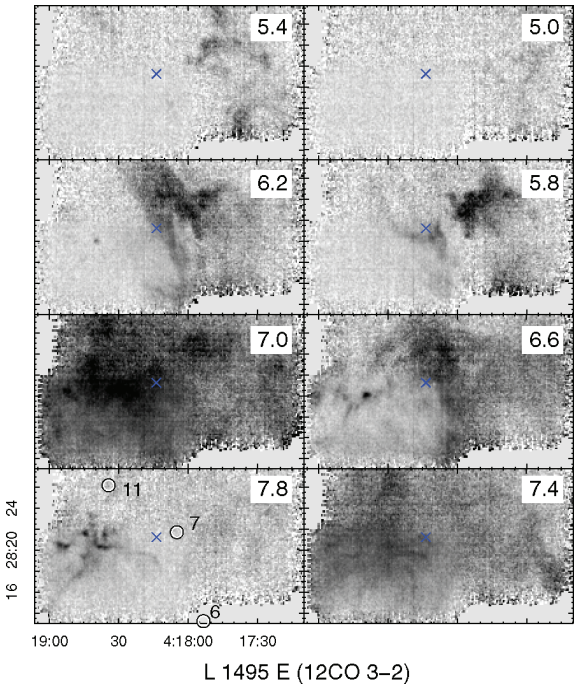

Figure 2. ^{13}CO 3–2 channel maps across L 1495 E, plotted between 4.8 and 8.0 km s^{-1}, in 0.4 km s^{-1} intervals. H^{13}CO$^+$ cores are marked and labelled bottom-left; the small cross in the centre of each map is drawn as a reference marker. The velocity of the channel is marked top-right in each panel.

The ^{13}CO and C^{18}O emission in the L 1495 E and L 1495 SE regions mapped is very weak; in ^{13}CO the peak intensity towards the compact features seen in Fig. 1 measures only $T_A^* \leq 2.0$ and ≤ 2.5 K, respectively. Profiles are generally narrow (∼2 km s^{-1} wide) and are either flat-topped or double-peaked (and therefore may in some regions be self-absorbed). ^{13}CO channel maps for both regions are shown in Figs 2 and 3 . Note the small group of compact, marginally redshifted knots to the east of cores 7 and 11 in the L 1495 E region, and the more diffuse, slightly blueshifted emission to the west and NW. Compact features are also evident along the SE ridge, at both blue and redshifted velocities. In both regions, however, with the possible exception of core 14 in Fig. 3, we again see no obvious correlation with the H^{13}CO$^+$ cores.

To illustrate the velocity structure observed in CO 3–2, we present in Figs 4–6 intensity-weighted radial velocity maps, colour-coded to show subtle changes in the centroid velocity of the gas (note that CO 3–2 line emission is detected at all locations in each image). These reveal the collimated blue- and redshifted lobes of a number of outflows in L 1495, but also large-scale velocity gradients and 'bubbles' of gas associated with clusters of young stars. In L 1495 E, for example, diffuse, redshifted emission envelopes the cluster of YSOs to the east of the H^{13}CO$^+$ cores 5–8 (Fig. 4 ; the YSOs are marked with crosses in this figure). CO velocities to the west and south of this chain of cores are more blueshifted (a result confirmed by the CO 1–0 observations of Goldsmith et al. 2008). The cluster of YSOs and the associated gas may be detaching itself from the

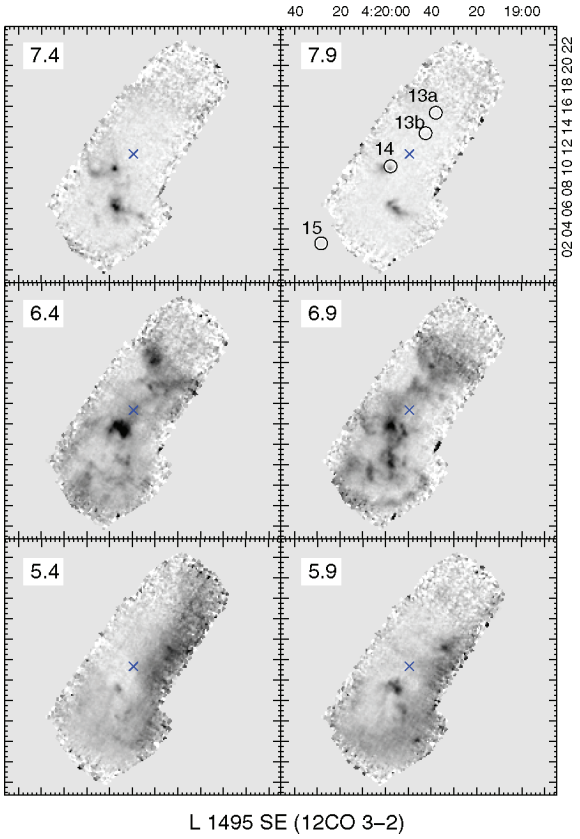

Figure 3. ^{13}CO 3–2 channel maps across L 1495 SE, plotted between 5.15 and 8.15 km s^{-1}, in 0.5 km s^{-1} intervals. H^{13}CO$^+$ cores are marked and labelled top-right; the small cross in the centre of each map is drawn as a reference marker. The velocity of the channel is marked top-left in each panel.

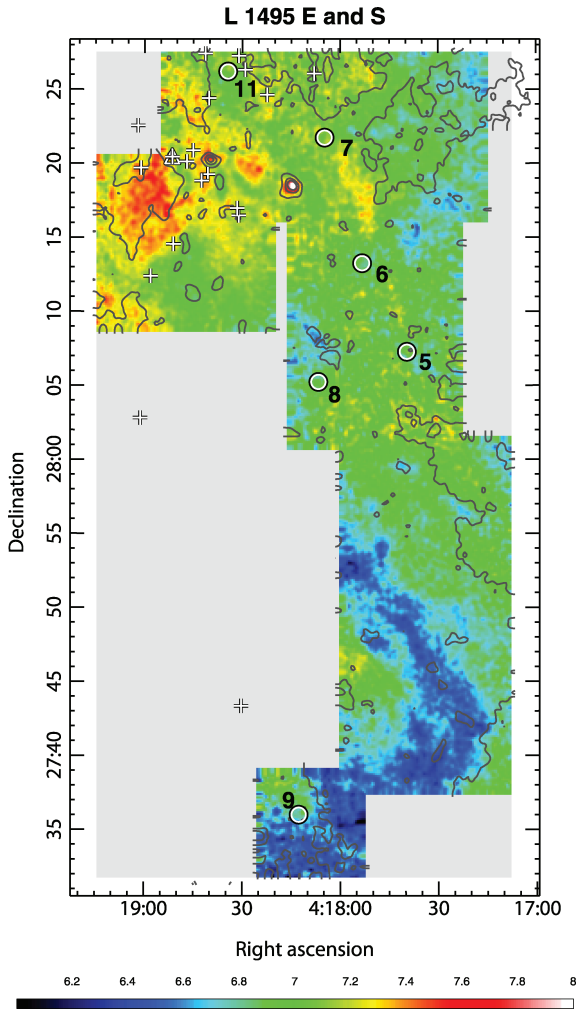

Figure 4. A plot of intensity-weighted radial velocity (first moment) showing the distribution of blue and redshifted CO 3–2 emission around L 1495 E and L 1495 S. Black/blue through to red/white display velocities in the range 6.0 to 8.0 km s^{-1} (green/yellow represent intermediate velocities). Circles, crosses and triangles mark the positions of H^{13}CO$^+$ cores (labelled), YSOs and HH objects, respectively. Integrated CO 3–2 emission (zeroth moment, from Fig. 1) is overplotted as contours; levels measure 4, 6, 8, 10, 12 K km s^{-1}. Note that there is CO 3–2 line emission throughout this entire map.

rest of the cloud; alternatively, the redshifted CO may represent a bubble being driven eastwards by the cluster of young stars.

In L 1495 W, H^{13}CO$^+$ core 4 seems to be surrounded by a number of young stars; those to the north coincide with a region of blueshifted CO, while those to the south coincide with a very distinct cloud of redshifted gas (Fig. 5). TTSs are often more widely distributed than their younger protostellar counterparts and pre-stellar cores; in L 1495 E and L 1495 W, we may therefore be witnessing the expansion of the natal cloud and the dispersal of these young stars.

We also note the east–west velocity gradient seen in the L 1495 N region. The map in Fig. 5 suggests that the diffuse background emission to the NW of the L 1495 bowl – in the unobserved regions in the centre and top of the figure – is likely to be redshifted with respect to the denser material in the bowl. Again, this is evident in the CO 1–0 observations of Goldsmith et al. (2008).

Along the SE ridge, a number of collimated outflow lobes (discussed further below) are superimposed on to a ridge of diffuse CO. In the centre of Fig. 6, there is some indication that the south-west edge of the ridge is redshifted with respect to the north-east edge. The cores and YSOs in this area lie predominantly along the boundary between this blue- and redshifted gas. If the cores and young stars delineate the high-density axis of the L 1495 ridge, then this distribution of blueshifted and redshifted gas could be symptomatic of rotation.

3.2 Averaged spectra and PV diagrams

Averaged spectra and position–velocity (PV) diagrams are shown in Figs 7 and 8. The former illustrates the relatively quiescent nature of the bulk of the gas in L 1495. They also give an indication of the mean opacity in the three lines observed. If the gas is optically thin, then the line intensity ratios at a given velocity should approach the abundance ratios, X[^{12}CO/^{13}CO]=70 and X[^{13}CO/C^{18}O]=8.4 (Frerking, Langer & Wilson 1982; Wilson 1999), provided that the excitation temperature and beam efficiency and filling factors are the same for all three lines. Photo-dissociation and chemical fractionation effects in low-extinction regions can also lead to enhanced isotopic ratios (Langer et al. 1989). At intermediate velocities (5–8 km s^{-1}), where line emission is detected in all three isotopologues, the ^{13}CO/C^{18}O line ratio is indeed close to this canonical value (see lower panels in Fig. 7). However, at these velocities, the ^{12}CO/^{13}CO ratio is of the order of 5–10, so the ^{12}CO emission is

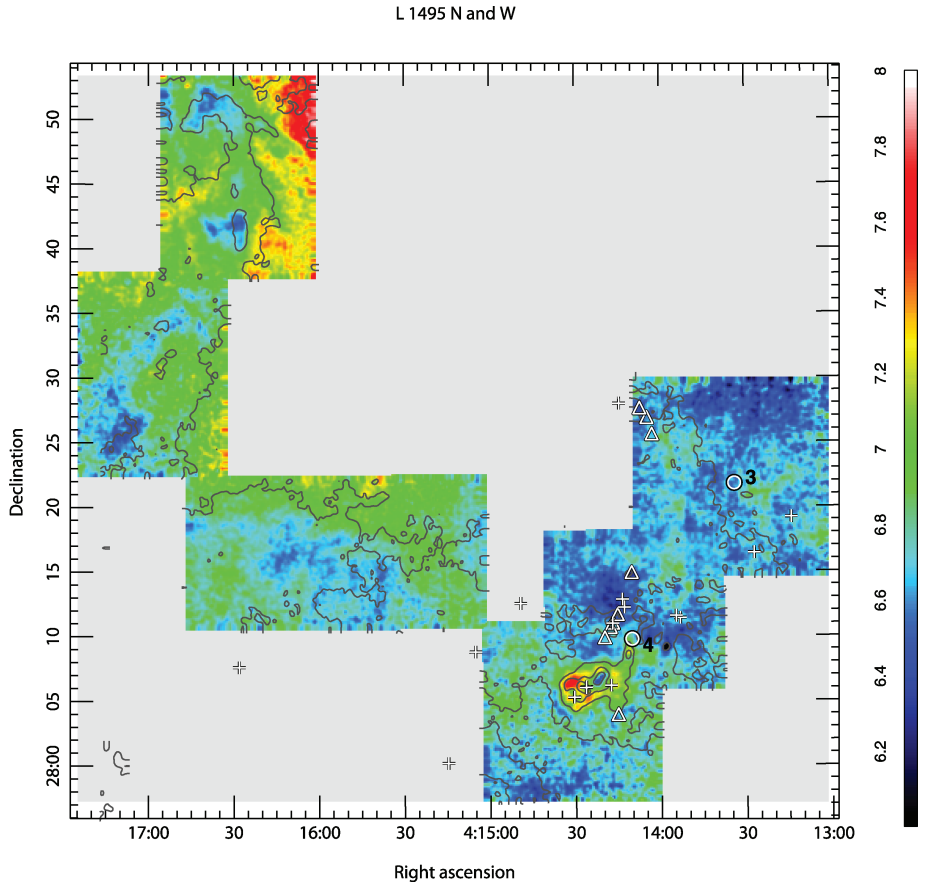

Figure 5. Same as Fig. 4, but for the region labelled L 1495 N and L 1495 W in Fig. 1. Again, there is CO 3–2 line emission throughout this region.

clearly optically thick. For a ^{12}CO/^{13}CO abundance ratio of 70, the ^{12}CO opacity, τ_{12}, is given by

$$\frac{\int T_{\rm A}^{*}(^{12}{\rm CO})\delta v}{\int T_{\rm A}^{*}(^{13}{\rm CO})\delta v} = \frac{(1-{\rm e}^{-\tau_{12}})}{(1-{\rm e}^{-\tau_{13}})}, \quad (1)$$

where $\tau_{13} = \tau_{12}/70$. A ^{12}CO/^{13}CO line ratio of $\sim$10 thus results in $\tau_{12} \sim 7.4$. Again, this value will be overestimated since ^{12}CO is almost certainly self-absorbed; a lower abundance ratio (e.g. Goldsmith et al. 2008) would also result in a lower opacity. The ratio does increase towards blueshifted and, particularly, redshifted velocities. It therefore seems likely that, in the extended regions where the bulk of the outflowing gas is found, the high-velocity line emission used to calculate the outflow parameters listed below will be only marginally optically thick.

PV diagrams, some of which are shown in Fig. 8, are useful for distinguishing compact molecular outflows from turbulent motions in the large-scale cloud. The outflows are seen as discrete horizontal spikes; turbulence appears as regions of diffuse emission that are more extensive along the spatial axis (vertically in these plots) though confined to low velocities, i.e. to within a few km s^{-1} of the ambient gas velocity. Indeed, we suggest that 'eyeballing' outflows in PV diagrams is a relatively reliable way of finding them in HARP data cubes, since they are spatially (in one axis at least) as well as spectrally distinct from turbulent cloud motions and multiple cores seen along the same sight-line.

We have therefore searched for outflows by stepping through our data cubes in latitude and then in longitude, identifying spikes in PV space that extend more than $\pm$2.5 km s^{-1} from the local ambient velocity with an intensity of >0.3 K (roughly the 2σ level). A spike is defined as being narrower than 1 arcmin in the spatial direction (i.e. in longitude and/or in latitude); we adopt 1 arcmin as a conservative upper limit to the width of an outflow lobe. Outflows are subsequently verified in redshifted and blueshifted integrated intensity maps, most of which are presented in the next section.

A number of outflows are evident in Figs 8. In the L 1496 E region, for example, a compact, redshifted knot of emission $\sim$8 arcmin to the west-south-west of CoKuTau-1, which we later refer to as E-CO-R1, is very distinct at declination $\sim$28°18′ in Fig. 8(a). This feature is also evident $\sim$5 arcmin SE of core 7 in Fig. 4. Similar, though less extreme spikes extending redwards and bluewards of the ambient gas are seen to the north of V892 Tau (not shown, though discussed further below). Fig. 8(b) is typical of PV diagrams further west, towards the centre of the L 1495 bowl, where we find no clear-cut examples of molecular outflows, though where the gas generally appears more turbulent. This is particularly true in the region labelled L 1495 N in Fig. 1, where the emission profiles are double-peaked (top section in Fig. 8c). The CO 3–2 emission appears somewhat more ordered to the south and west of this region [see e.g. Fig. 8c (lower section) and Fig. 8d].

Along the SE ridge in L 1495, PV spikes associated with high-velocity outflows are more prevalent. Example PV diagrams, again plotted along the declination axis, are presented in Figs 8(e) and (f): these show emission from the complex HH 392 region and the red lobe of the collimated bipolar outflow associated with IRAS 04166+2706 and core 13b, respectively (discussed further below).

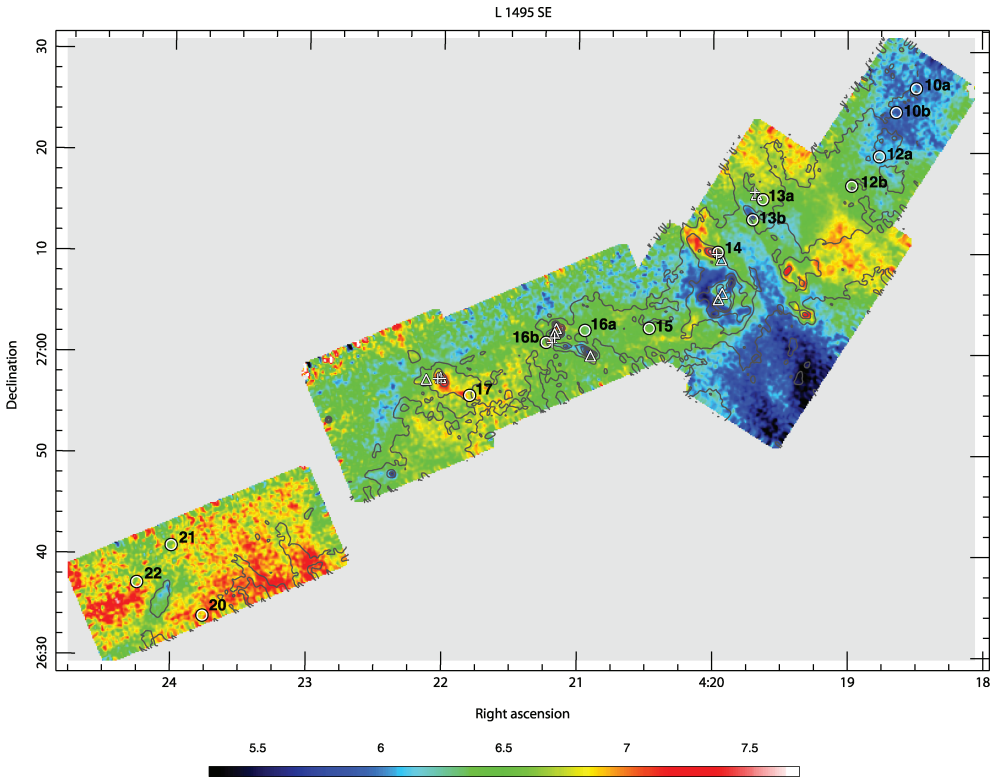

Figure 6. Same as Fig. 4, but for the SE ridge in L 1495. In this region, the colours span 5.3 km s^{-1} (black/blue) to 7.7 km s^{-1} (red/white). Once again, we detect CO 3–2 line emission throughout this entire region.

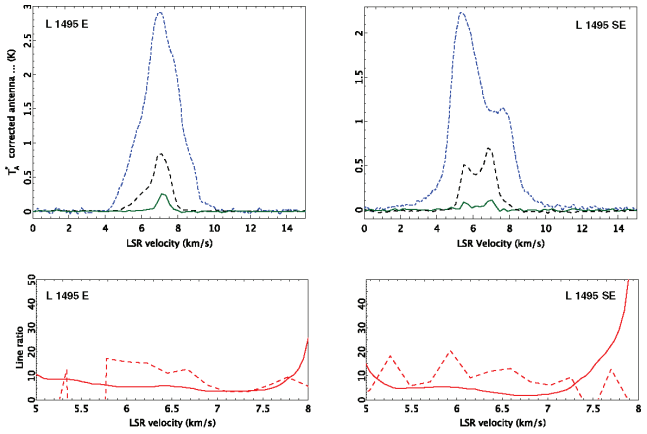

Figure 7. Top: ^{12}CO 3–2 (blue/dot–dashed), ^{13}CO 3–2 (black/dashed) and C^{18}O 3–2 (green/full) spectra, averaged over the full extent of the areas mapped simultaneously in ^{13}CO and C^{18}O in L 1495 E and L 1495 SE. The ^{13}CO and C^{18}O spectra have been binned to a resolution of 0.25 km s^{-1}; the resolution of the ^{12}CO 3–2 spectra is 0.05 km s^{-1}. Bottom: ratio of these averaged spectra; ^{12}CO/^{13}CO full red lines, ^{13}CO/C^{18}O dashed red lines.

3.3 Outflows in L 1495

When trying to identify outflows in complex regions like L 1495 one ideally needs a measure of the systemic velocity associated with each outflow driving source. This is difficult to do using the CO 3–2 observations alone (Fig. 8); even the ^{13}CO and C^{18}O profiles are double-peaked in some regions (Fig. 7). We therefore use the H^{13}CO$^+$ observations of OMK02 as a guide; these data are more likely to be optically thin and trace only the quiescent, high-density gas in each area. Cores are mapped throughout the bowl and SE ridge in L 1495. The H^{13}CO$^+$ data also suggest that the ambient velocity does not change drastically across the region (Table 1), a result which is supported by our CO 3–2 observations (particularly when one scans through the CO 3–2 data cubes in PV space), and our more optically thin, though less-extensive, ^{13}CO and C^{18}O data (Figs 2 and 3).

When constructing integrated intensity maps of the high-velocity blue and redshifted gas, we therefore adopt systemic velocities of 7.0, 6.7 and 6.6 km s^{-1} for the L 1495 E, L 1495 W and L 1495 SE regions, respectively. Contour maps for select regions are presented in Figs 9–12, where we also overplot the positions of the Taurus YSOs, known HH objects and H^{13}CO$^+$ cores for reference.

In these figures, we make use of shallow though extensive near-IR images of Taurus, obtained as part of the UK Infrared Deep Sky Survey currently being conducted at the United Kingdom Infrared Telescope (UKIDSS: Lawrence et al. 2007). Images in broad-band K and narrow-band H_2 2.122 μm emission (hereafter referred to simply as H_2) have been secured for the entire Taurus-Auriga-Perseus complex. The wide-field camera (WFCAM) used to obtain these data, the data reduction procedure and the WFCAM archive are described in detail by Lucas et al. (2008) and Davis et al. (2008). Note that we also use the acronym 'MHO' for the molecular hydrogen emission-line objects – the shock-excited IR counterparts to HH

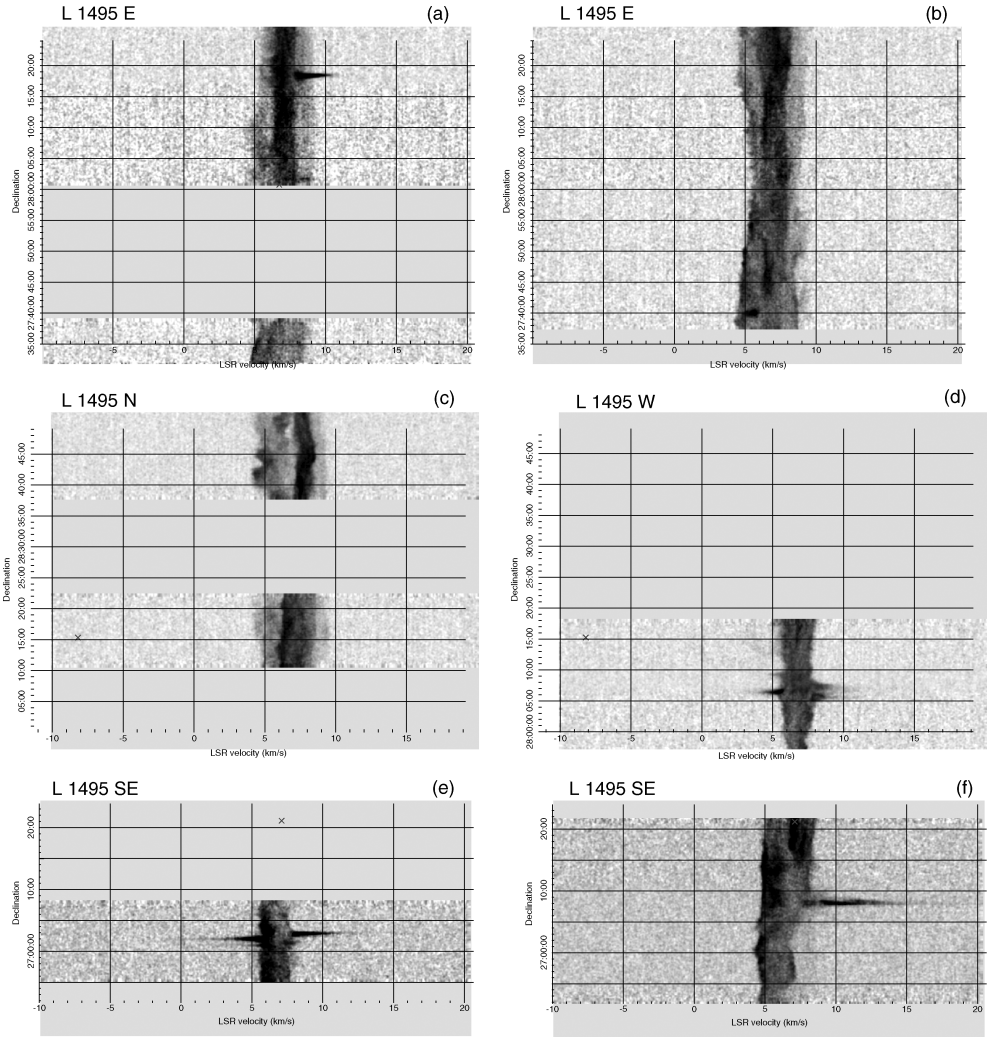

Figure 8. CO 3–2 PV diagrams measured along vertical slices through L 1495 E at RA 4:18:14.2 (a) and RA 4:17:30.1 (b), through L 1495 N at RA 4:16:30.2 (c), through L 1494 W at RA 4:14:22.2 (d), and through L 1495 SE at RA 4:21:11.1 (e) and RA 4:19:28.7 (f).

objects – observed in L 1495.[2] A complete catalogue of all known galactic MHOs is available online[3] and in Davis et al. (2010).

Below we discuss the star-forming regions in L 1495 individually.

3.3.1 L 1495 E: CoKu Tau-1 and HH 156

L 1495 E harbours a cluster of about a dozen TTSs, many of which have been identified through X-ray observations (the V 410 X-ray and Anon# sources; Strom & Strom 1994). OMK02 label five cores in this region. In the integrated intensity maps in Fig. 1, the CO is diffuse and optically thick across much of the region; only a few compact peaks are detected, all of which are marginally redshifted and unrelated to the $H^{13}CO^+$ cores (Fig. 9, though note that the $H^{13}CO^+$ map does not cover the region south of the young star X-ray 7 and east of core 8).

Two seemingly unrelated redshifted knots are identified as molecular outflow features, E-CO-R1 and E-CO-R2. Neither is obviously related to any of the YSOs or $H^{13}CO^+$ cores; their progenitors remain unknown, although candidate sources surround E-CO-R1, and this object does coincide with a peak in our ^{13}CO integrated intensity map in Fig. 1. Note also that in the H_2 images we detect no line-emission features in this region.

In Fig. 9, CoKu Tau-1 seems to be associated with a third compact redshifted CO feature. However, this low-velocity knot of emission fails our search criteria for outflows (described above) and so is not identified as such here. CoKu Tau-1 does power HH 156 A and B, two compact HH objects offset ∼2 and ∼12 arcsec to the south-south-west; the CO peak could represent the counter-lobe, though deeper and/or higher resolution CO data are needed to be sure. (The lack of blueshifted CO around HH 156 may be a result of the HH flow exiting the cloud, or may be due to the dispersal of the core around this TTS.)

Apart from CoKu Tau-1, none of the young stars in the region are obviously driving CO outflows; presumably most are too evolved. Of the dozen YSOs to the east of cores 5–8 in Fig. 9, all bar three have neutral *Spitzer*-IRAC colours ([3.6]–[4.5]∼0; [5.8]–[8.0]∼0), consistent with relatively evolved (weak line) TTSs and an absence

[2]The acronym MHO has recently been approved by the International Astronomical Union (IAU) Working Group on Designations and has been entered into the Dictionary of Nomenclature of Celestial Objects (http://cdsweb.u-strasbg.fr/cgi-bin/Dic?MHO).

[3]http://www.jach.hawaii.edu/UKIRT/MHCat/

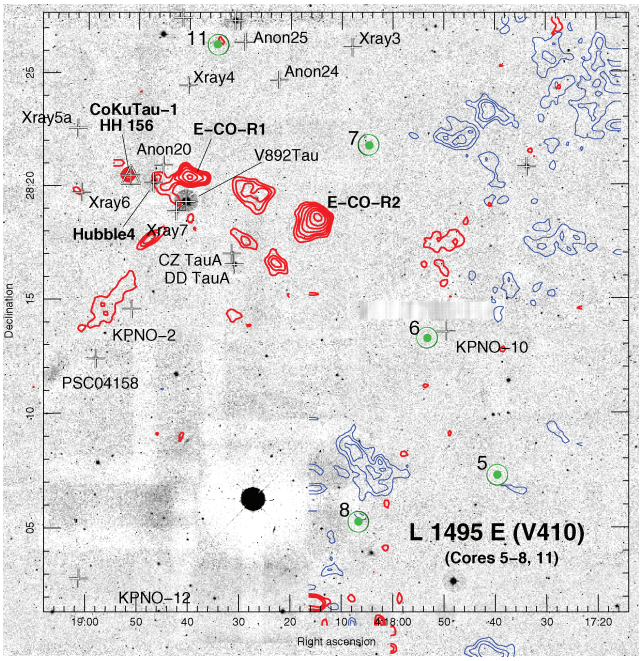

Figure 9. High-velocity CO 3–2 emission in L 1495 E, integrated between 4.0 and 6.0 km s^{-1} (blue/thin contours) and 8.0 and 10.0 km s^{-1} (red/thick contours), plotted as contours on top of a narrow-band H_2 (+ continuum) image of the region; contour levels are 1.75, 2, 2.5, 3, 4, 5, 7, 10 K km s^{-1}. Green circles, crosses and triangles mark $H^{13}CO^+$ cores, YSOs and HH objects, respectively.

of mid-IR excess due to a lack of circumstellar material (Luhman et al. 2006, note that V 892 Tau is saturated). Only CoKu Tau-1, CZ TauA and DD Tau A have Two Micron All Sky Survey (2MASS) near-IR and *Spitzer* mid-IR magnitudes that brighten towards longer wavelengths, consistent with them being protostars or very young TTSs and therefore possible molecular outflow candidates. This low number of protostars in L 1495 E is consistent with the paucity of outflows in our H_2 and CO data.

3.3.2 L 1495 W: CW Tau and HH 220/826-828

The high-velocity CO in L 1495 W is shown in Fig. 10. Again, the positions of candidate YSOs are marked, although note that the *Spitzer* observations of Luhman et al. (2006) do not cover this region. The most dramatic feature in this area is the bubble of redshifted gas that surrounds a small group of young stars, YSOs 1, 2, 3[4] and CIDA-1 (see also Fig. 5). More compact blueshifted features are also observed in L 1495 W.

At least four molecular outflows exist in this region: (i) a compact north–south bipolar flow, W-CO-flow1, centred ∼1 arcmin south of (and seemingly unrelated to) $H^{13}CO^+$ core 4, (ii) a collimated blueshifted lobe extending north-westwards from YSOs 1 and 2 (which presumably also drive some [or all] of the redshifted CO to the SE), (iii) a compact blueshifted CO feature, W-CO-B1, associated with HH 828, and (iv) a second blue CO knot, W-CO-B2, to the south-west of core 4, which may well be driven by IRAS 04108+2803A; this CO knot is certainly extended towards this object, which is also rather red ($J - H = 3.10$, $H - K_s = 2.32$).

Two additional flows are detected in HH and H_2 emission, HH 220/826, a jet from CW Tau (McGroarty & Ray 2004), and an arc of HH/H_2 emission, HH 827/MHO 715, which may be associated with low-velocity redshifted CO extending southwards from CIDA-1 (though again this emission fails our outflow criteria).

YSO 1/2, YSO 3 and CIDA-1 have near-IR 2MASS colours consistent with youth. The TTSs CW Tau, V773 Tau A and FM Tau are more evolved and appear to be associated with a completely separate region of star formation. CW Tau is thought to be the most active classical TTS in this region. Even so, we detect no H_2 line emission from its HH objects, and only HH 828 appears to be associated with high-velocity (blueshifted) CO emission.

3.3.3 L 1495 SE: HH 390-391

The lower portion of the L 1495 ridge is populated with a number of young stars and HH flows. The area around cores 13a, 13b, 14 and 15 is shown in Fig. 11. Two of these four $H^{13}CO^+$ cores (13b and 14) are associated with *IRAS* sources and HH objects.

IRAS 04169+2702 (core 14) drives a collimated, possibly precessing bipolar molecular outflow and HH object (HH 391A); the HH object is also identified in H_2 emission, MHO 731 (see also Gomez et al. 1997).

A second, rather spectacular bipolar CO outflow emanates from core 13b. This flow is particularly striking in Fig. 6. The source of the outflow, IRAS 04166+2706, is identified at submm wavelengths (Santiago-García et al. 2009), though it does not appear in the 2MASS point source catalogue nor in the YSO lists of Luhman et al. (2006) and Kenyon et al. (2009). It must therefore be particularly young, as expected for molecular outflow and MHO progenitors (Hatchell et al. 2007b; Davis et al. 2008, 2009). Very faint H_2 features, MHO 717 A/B and MHO 718, are observed in both flow lobes. This outflow is well known from previous CO observations: Tafalla et al. (2004) report the discovery of a collimated, extremely high-velocity (EHV) outflow from IRAS 04166+2706, which Santiago-García et al. (2009) have since observed in SiO 2-1 emission. Both groups present CO 2-1 spectra with striking peaks in the line wings at −35 and +45 km s^{-1}. However, this EHV outflow component is only marginally detected (at the 2–3σ level) in our 3–2 data. Based on a noise level of T_A^*(rms) ∼ 0.1 K in our data (equivalent to a main beam brightness temperature of ∼0.2 K), we set an upper limit of ∼0.5 for the 3–2/2–1 intensity ratio (note that the beam sizes are comparable). This ratio suggests that the clumps or 'molecular bullets' associated with the EHV flow from IRAS 04166+2706 are relatively cold and/or diffuse ($n_{H_2} \leq 10^4$ cm^{-3}, $T \leq 50$ K; Yeh et al. 2008).

Core 13a drives a much less well-defined molecular outflow. MHO 716 may be associated with a redshifted outflow lobe; HH 390 (which extends towards the south-west; Gomez et al. 1997) would then be excited in the blue lobe. The 2MASS source J04194148+2716070, which Luhman et al. (2006) and Kenyon et al. (2009) misidentify as IRAS 04166+2706, is situated ∼50 arcsec to the north-east of core 13a, and is a possible driving source for this outflow.

Considering these three cores (13a, 13b and 14) and their associated YSOs together, IRAS 04166+2706 is presumably the youngest of the three; this is consistent with its powerful EHV CO outflow, its H_2 shocks, and the *absence* of HH objects. IRAS 04169+2702 is probably somewhat more evolved, having IR colours that are

[4]Kenyon et al. (2009) refer to these objects as MHO 1, MHO 2 and MHO 3, using the acronym MHO for 'Mill House Observatory'. We identify these sources with YSO so as to distinguish them from MHOs.

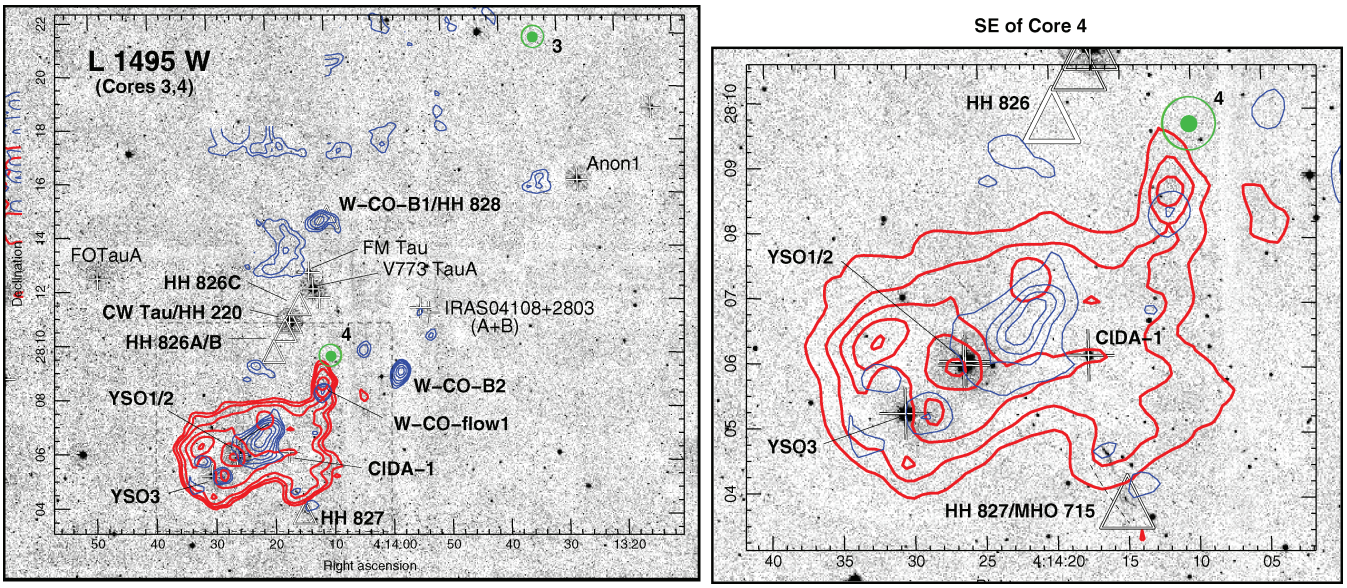

Figure 10. Same as in Fig. 9, but for the L 1495 W region. Left-hand panel: high-velocity CO 3–2 integrated between 3.7 and 5.7 km s^{-1} (blue/thin contours) and 7.7 and 9.7 km s^{-1} (red/thick contours). Contour levels are 1.0 (blueshifted only), 1.2, 1.5, 2, 3, 4, 5, 7, 10 K km s^{-1}. Right-hand panel: a close-up view of the region to the SE of core 4 (marked with a dashed square at left); contours measure 1, 2, 3, 4, 5, 7, 10 K km s^{-1}.

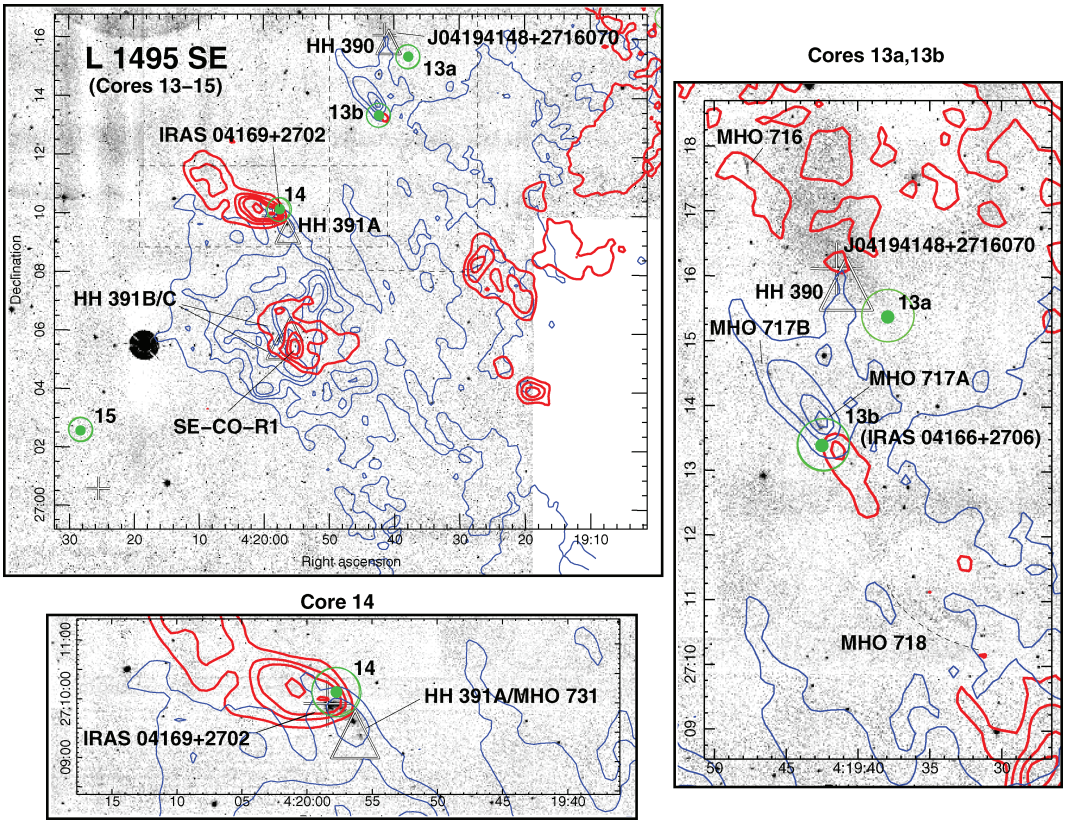

Figure 11. Same as in Fig. 9, but for the region around cores 13–15 in L 1495 SE. Top left: high-velocity CO 3–2 integrated between 3.6 and 5.6 km s^{-1} (blue/thin contours) and 7.6 and 9.6 km s^{-1} (red/thick contours); levels are 2, 3, 4, 5, 7, 10 K km s^{-1} for both blue- and redshifted emission. Right and bottom left: close-up views of the outflows associated with cores 13a,13b and 14: contour levels are 1.5 (red only), 2, 3, 4, 5, 7, 10 K km s^{-1} in the former and 2, 3, 4, 7, 10 K km s^{-1} in the latter.

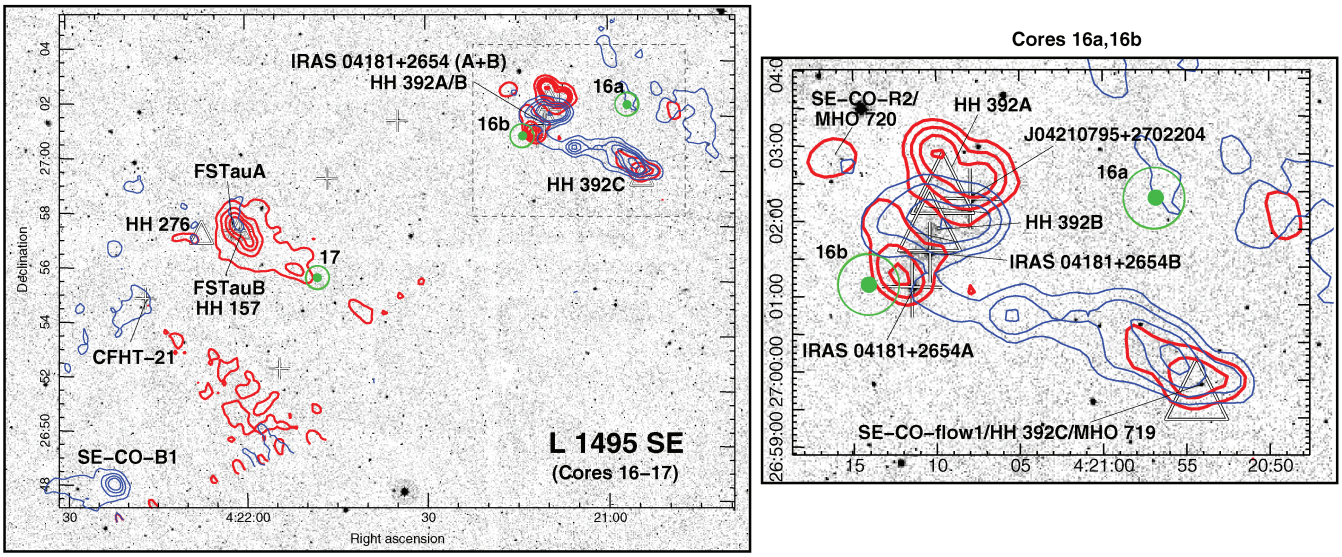

Figure 12. Same as Fig. 9 but for the region around cores 16a,16b and 17 in L 1495 SE. *Left* - high-velocity CO 3–2 integrated between 3.6 and 5.6 km s^{-1} (blue/thin contours) and 7.6 and 9.6 km s^{-1} (red/thick contours); levels are 1,2,3,4,5,7,10 K km s^{-1} for both blue- and redshifted emission. *Right* - a close-up of the outflows associated with cores 16a and 16b; contour levels are 1,2,4,7,10 K km s^{-1}.

consistent with a Class I protostar ($H - K_s = 2.6$; [3.6]–[5.8] = 2.1). J04194148+2716070 is bluer and is almost certainly a TTS, which would explain its association with an HH object and the lack of well-defined CO 3–2 outflow lobes.

Further south, HH 391 B and C represent a chain of optical features that extend over ∼1 arcmin in a north–south direction (Gomez et al. 1997). These objects coincide with large, complex bubbles of both blue- and redshifted emission. HH 391 B/C are unlikely to be associated with the IRAS 04169+2702/HH 391 A outflow. No H_2 emission was detected in this region, and the relationship between these shock features and the complex CO emission in this area is unclear, although high-velocity CO does coincide with these objects (we label the more clearly defined redshifted emission SE-CO-R1). Moreover, a ^{13}CO peak does coincide with HH 391 B/C in our integrated intensity map in Fig. 1, which may be a sign of youth.

3.3.4 L 1495 SE: FS Tau A/B (Haro 6-5B) and HH 157/276/392

Moving further SE along the L 1495 ridge, molecular outflows are detected around IRAS 04181+2654 and the well-studied FS Tau A/B (Haro 6-5B) system (Fig. 12).

IRAS 04181+2654 A is closest to core 16b and appears to drive a bipolar CO outflow in a roughly east–west direction. The blue lobe of this flow may overlap with a second bipolar outflow, SE-CO-flow1, which drives the compact shock features HH 392 C/MHO 719. There is no source candidate for SE-CO-flow1 in the 2MASS or *IRAS* point source catalogues, and Luhman et al. (2006) and Kenyon et al. (2009) do not identify a YSO near these objects. IRAS 04181+2654 A is resolved by 2MASS and exhibits an excess consistent with a protostar ($J - H = 3.58$, $H - K_s = 2.30$).

IRAS 04181+2654 B lies ∼30 arcsec NW of star A; this nebulous IR source is associated with an arc of HH emission, HH 392 B (tentatively detected here in H_2) and also possesses considerable excess in the near-IR ($J - H = 5.11$, $H - K_s = 2.70$). The third source in the region, 2MASS source J04210795+2702204, has less extreme near-IR colours ($J - H = 1.8$, $H - K_s = 1.5$), though may none the less also contribute to the complex high-velocity CO evident in Fig. 12. The 'kidney' shape of the blue- and redshifted features coincident with HH 392 A and B certainly suggest the presence of multiple flow lobes.

Approximately 1.5 arcmin to the north-east of IRAS 04181+2654, there is a faint knot of H_2 emission, MHO 720, which coincides with a knot of redshifted CO, SE-CO-R2 and a very marginal detection of blueshifted CO offset ∼15 arcsec to the south-west. In all, there are at least four molecular outflows within a 5-arcmin radius of cores 16a and 16b.

FS Tau A ($J - H = 1.47$, $H - K_s = 1.73$) and FS Tau B ($J - H = 1.06$, $H - K_s = 1.60$; also known as Haro 6-5B) are a pair of TTSs, the latter being associated with the spectacular HH jet and bow shock HH 157 (Eislöffel & Mundt 1998). We detect redshifted CO emission from this outflow, though no H_2 line emission. HH 276 is a chain of faint HH knots that crosses the HH 157 jet ∼1 arcmin to the north-east of FS Tau B, although no high-velocity CO is clearly identified from this flow.

Lastly, SE of FS Tau A, we note the very tentative detection of a bipolar CO outflow from CFHT-21, orientated NE–SW, roughly parallel with the FS Tau B jet. This marginal detection is consistent with the near-IR colours of this TTS ($J - H = 1.5$, $H - K_s = 1.0$). SE-CO-B1 is a compact though massive high-velocity knot with a tail extending along the SE ridge. This feature is, however, not related to any known YSOs in the region.

3.4 Outflow parameters

The physical parameters for the molecular outflows described above are listed in Table 2 (we also list HH outflows not detected in high-velocity CO emission). The mass in the molecular outflow lobes (the mean of both lobes if the outflow is bipolar) is derived from the column density integrated across the extent of the high-velocity line wings, which in turn is calculated from the integrated antenna temperature, corrected for the main-beam efficiency (we assume a beam filling factor of unity), and an estimate of the CO 3–2 excitation temperature.

The excitation temperature, T_{ex}, in the ambient gas can be estimated from the peak temperature in the CO 3–2 line profiles, provided the gas is optically thick though not self-absorbed (Pineda,

Table 2. Parameters for the outflows in L 1495.

YSO or outflow[a]	Area[a]	YSO type[a]	RA[a] (J2000.0)	Dec [a] (J2000.0)	CO flow[b]	HH/MHO[c]	$H^{13}CO^+$ core[c]	M [d] ($M_\odot$)	$\lvert v_o - v\rvert$ [d] (km s^{-1})	P[d] ($M_\odot$ km s^{-1})	E[d] ($\times 10^{34}$ J)
CoKu Tau-1	E	TTS	4:18:51.5	28:20:26	No?	HH156		–	–	–	–
E-CO-R1[e]	E	–	4:18:39.5	20:20:20	Red			0.0098	2.3	0.022	5
E-CO-R2[e]	E	–	4:18:15.0	28:18:30	Red			0.0256	4.0	0.102	41
YSO 1/2	W	Class I	4:14:26.3	28:06:03	Bipolar			0.0156	4.7	0.074	35
CIDA-1	W	TTS	4:14:17.6	28:06:10	No?	HH827/MHO715		–	–	–	–
CW Tau	W	TTS	4:14:17.0	28:10:58	No?	HH220/826		–	–	–	–
W-CO-B1[e]	W	–	4:14:10.7	28:14:40	Blue	HH828		0.0028	3.1	0.009	3
W-CO-flow1[e]	W	–	4:14:12.0	28:08:30	Bipolar		4?	0.0038	3.1	0.012	4
IRAS 04108+2803A?	W	Class I	4:13:57.4	28:09:10	Blue			0.0055	3.3	0.018	6
J04194148+2716070	SE	TTS	4:19:41.5	27:16:07	No	HH390/MHO716	13a?	–	–	–	–
IRAS 04166+2706[f]	SE	Class 0?	4:19:42.4	27:13:24	Bipolar	MHO717/718	13b	0.0217	8.9	0.193	172
IRAS 04169+2702	SE	Class I	4:19:58.5	27:09:57	Red	HH391A/MHO731	14	0.0301	6.1	0.184	112
SE-CO-R1	SE	–	4:19:52.5	27:05:30	Red?	HH391B/C		0.0592	6.2	0.367	228
SE-CO-R2	SE	–	4:21:17.1	27:02:50	Red	MHO720		0.0021	2.6	0.005	1
J04210795+2702204	SE	Early TTS	4:21:08.0	27:02:20	Bipolar	HH392A		0.0157	5.4	0.085	46
IRAS 04181+2654A	SE	Class I	4:21:11.5	27:01:09	Red?		16b	0.0049	2.6	0.013	3
IRAS 04181+2654B	SE	Class I	4:21:10.4	27:01:37	?	HH392B	16b?	–	–	–	–
SE-CO-flow1[e]	SE	–	4:20:56.0	27:00:00	Bipolar	HH392C/MHO719		0.0153	3.2	0.049	16
FS Tau B	SE	Early TTS	4:22:00.7	26:57:32	Red	HH157		0.0209	4.9	0.102	50
CFHT-21[g]	SE	TTS	4:22:16.8	26:54:57	Bipolar?			–	–	–	–
SE-CO-B1[e]	SE	–	4:22:22.0	26:48:00	Blue			0.0251	3.8	0.095	36

Note. The top nine flows are in the bowl; the remaining flows are in the SE ridge.

[a]The most likely driving source of the CO outflow, the area in which it is found in L 1495, its YSO type (based on near- and/or mid-IR colours) and its coordinates. If no YSO source is identified, the label used for the CO outflow or high-velocity CO peak is given. The coordinates then refer to the approximate midpoint between the bipolar lobes, or the peak in the CO emission if the flow is monopolar.

[b]Indication of whether the CO outflow is bipolar or monopolar (with a redshifted or blueshifted lobe clearly defined). 'No' in this column indicates that no CO outflow was detected.

[c]Associated HH objects, MHOs and $H^{13}CO^+$ core (from OMK02).

[d]The mass, maximum radial velocity (the difference between the nominal ambient velocity and the velocity in the line wings at the 2σ noise level); the momentum and the kinetic energy of each outflow lobe. Mean values are quoted if the flow is bipolar.

[e]CO outflows with no *clearly identified* driving source.

[f]Driving source not listed in the YSO catalogue of Luhman et al. (2006), Kenyon et al. (2009) or detected by 2MASS.

[g]CO outflow only a marginal detection; requires confirmation with deeper observations.

Caselli & Goodman 2008; Buckle et al. 2010). However, T_{ex} in the ambient gas is not necessarily the same as T_{ex} in the entrained outflow gas, where the kinetic temperature may be higher and the gas is almost certainly compressed as it is swept up by the underlying jet and HH/MHO bow shocks (e.g. Hatchell et al. 1999; Davis et al. 2000a; Giannini et al. 2001; Lee et al. 2002; van Kempen et al. 2009). We therefore adopt a somewhat higher value than is implied by (i) the average CO 3–2 spectra in Fig. 7 ($T_A^* \sim 3$ K; $T_{ex} \sim 11$ K), which include the more diffuse regions away from the central SE ridge and star-forming cores, or (ii) the brightest spectra observed in L 1495 ($T_A^* \sim 17$ K; $T_{ex} \sim 35$ K).[5] We instead use a value of 50 K, consistent with the range in excitation temperature derived from CO line ratios in other outflows – albeit assuming optically thin emission (e.g. Davis et al. 1998; Hatchell et al. 1999; Davis et al. 2000a; van Kempen et al. 2009). The mass is in any case relatively insensitive to temperature, varying by only 40 per cent over the temperature range 20–100 K (Hatchell et al. 2007a). Assuming an abundance of $X_{CO} = 10^{-4}$ (Frerking et al. 1982; Wilson 1999), the column density (in units of cm^{-2}) is then given by $N_{H_2} = 2.5 \times 10^{19}(\int T_b^* dv)$, where the integrated line wings are in units of K km s^{-1} (Hatchell et al. 2007a). $\int T_b^* dv$ is measured from the integrated high-velocity blueshifted and redshifted outflow maps used to plot the contours in Figs 9–12; the integrated flux measured in an ellipse that envelopes each outflow lobe is 'sky subtracted' using the flux measured in an outer annulus (this eliminates diffuse redshifted or blueshifted gas not associated with the outflow); the derived column density is then scaled by the HARP beam size and the factor $1.3 \times m_{H_2}$ (where m_{H_2} is the mass of an H_2 molecule) to give the mass in each outflow lobe.

We assume that the wings of the CO 3–2 emission are optically thin, so the values in Table 2 will be lower limits: the mass, M, momentum, P, and kinetic energy, E, are probably underestimated by a factor of 2–4 (Cabrit & Bertout 1990; Hatchell et al. 2007a). Furthermore, the radial velocity, $|v_o - v|$ (v is the velocity in the line wings where the emission reaches the 2σ noise level; v_o is the ambient velocity from Table 1), used to calculate the momentum and energy, will also be underestimated, by a factor $1/\sin i$, where i is the inclination angle with respect to the plane of the sky. Obviously for flows close to the plane of the sky, this factor can be quite considerable, although flows with $i \gg 60^\circ$ will be difficult to

[5]In an isothermal slab, assuming local thermodynamic equilibrium and optically thick emission, the excitation temperature, T_{ex}, is related to T_b, the line peak main beam brightness temperature, by: $T_{ex}(3\text{–}2) = 16.59/\ln[1 + 16.59/(T_b(^{12}CO) + 0.036)]$ (Pineda et al. 2008).

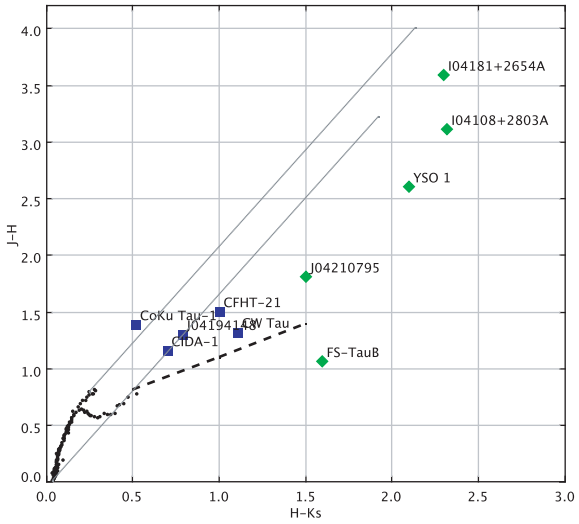

Figure 13. Near-IR colour–colour (CC) diagram for the HH jet and molecular outflow sources in L 1495, which are marked with blue squares and green diamonds, respectively. The black dots lower left represent the locus of intrinsic colours for main-sequence dwarfs and giants (Koornneef 1983); the dashed line indicates the locus of TTSs (Meyer, Calvet & Hillenbrand 1997). The full parallel lines are reddening vectors for the main-sequence stars up to $A_v = 30$ mag (Rieke & Lebofsky 1985).

detect in our CO observations; for an inclination angle of 60°, P and E will be underestimated by an additional factor of 2 and 4, respectively. Even so, the parameters listed in Table 2 are not unusual for outflows from low-mass young stars. They are marginally lower than (within an order of magnitude of) those typically observed for low-mass YSO outflows in Orion, Ophiuchus and Perseus (e.g. Knee & Sandell 2000; Williams, Plambeck & Heyer 2003; Arce & Sargent 2006; Bussmann et al. 2007; Stanke & Williams 2007).

4 DISCUSSION

4.1 Using outflows to distinguish starless from protostellar cores in L 1495

L 1495 contains the largest concentration of young stars in the Taurus region. The majority of these are found in the L 1495 bowl, particularly the denser eastern half of the bowl (the molecular gas in the western bowl region is more extensive and generally more diffuse; Goldsmith et al. 2008) and in the lower half of the SE ridge (Luhman et al. 2006; Kenyon et al. 2009). The low number-density of YSOs in the upper, north-western half of the ridge, where OMK02 nevertheless find a number of massive, dense cores (9a, 9b, 10a, 10b and 12), suggests that star formation has yet to take place in this area. The absence of HH objects, MHOs and CO outflows in this region supports this interpretation.

The molecular outflows in L 1495 are listed in Table 2, along with associated HH objects, MHOs, $H^{13}CO^+$ cores and candidate YSO driving sources. YSO source classifications are based on near-IR and/or mid-IR photometry (as described in section 1). In Fig. 13 we plot the 2MASS colours of the HH jet and outflow sources in Table 2 on a near-IR CC diagram. As expected, the majority of the sources lie to the right of the reddening band (the two parallel lines), although notably the sources with no CO outflow all lie in the region associated with TTSs, while the young stars that do drive molecular outflows are all much redder (in both $J-H$ and $H-K_s$). Clearly the molecular outflow-driving sources are more embedded than their HH jet-driving counterparts.

Of the 22 cores labelled in Fig. 1, only four – 13a, 13b, 14 and 16b – appear to be associated with YSOs (in each case the YSO is located within the 50 per cent integrated intensity contour in the $H^{13}CO^+$ maps). This relatively small fraction of cores with YSOs is consistent with the rest of Taurus; OMK02 find that only 22 per cent of their condensations are associated with embedded sources. In L 1495, these 'cores harbouring stars' certainly seem to be protostellar; at least three of the four cores (13b, 14 and 16b) are associated with molecular outflows; the CO flow from 13a is a marginal detection, though this core is also probably associated with an HH jet and MHO. As has been noted in other outflow surveys (e.g. Davis et al. 2008; Hatchell & Dunham 2009), this suggests that CO outflows are useful tracers of the locations of protostellar cores. Indeed, outflow surveys may be used in combination with near- and mid-IR photometric studies of star-forming regions to establish more accurately the fraction of cores that do harbour accreting protostars.

Spitzer, when combined with near-IR data from e.g. 2MASS or WFCAM, can be a powerful tool for searching for Class 0/I protostars (although saturation can be a problem with *Spitzer* data, particularly at longer wavelengths). This is especially true in nearby, low-mass star-forming regions like Taurus, where extinction and crowding are minimal (Evans et al. 2009). A few recent studies have revealed the presence of extremely faint protostellar objects inside a handful of cores that were previously thought to be starless (Crapsi et al. 2005; Bourke et al. 2006). But such low-mass cores may be below the resolution and sensitivity limits of the $H^{13}CO^+$ survey discussed here, and these objects are unlikely to drive powerful CO outflows or bright H_2 jets. The YSO list, derived from optical, near-IR and mid-IR photometry and spectroscopy (Kenyon et al. 2009), is therefore expected to be relatively complete for the core mass range under scrutiny here.

A number of high-velocity CO features appear to be without driving sources in Table 2. In some cases, their progenitors may be nearby; however, in a few (W-CO-flow1, SE-CO-flow1 and SE-CO-R1/HH 391), the location of the driving source is clearly defined, yet they are still undetected. These flows are probably driven by Class 0 sources which require deeper mid-IR or far-IR/submm observations (Jørgensen et al. 2007, 2008).

From our comparison of the $H^{13}CO^+$ cores mapped by OMK02 to the YSO source list and outflows mapped here, at first sight the ratio of starless cores to protostellar cores in L 1495 seems to be high; as noted earlier, of the 22 cores located in L 1495, only four appear to be coincident with known YSOs (although all are associated with outflows).

However, two cores, 3 and 4, are found in a region that was not observed with *Spitzer*. Luhman et al. (2006) estimate that pre-*Spitzer* studies of the YSO population in Taurus are only complete to about 80 per cent. They also point out that *Spitzer* is very well suited to finding disc-bearing stars down to masses of the order of 0.01 $M_\odot$ through considerable amounts of extinction ($A_v \sim 100$). The observations of OMK02 are sensitive to core masses in the range $3.5\,M_\odot < M < 20.1\,M_\odot$. Even for a very low star formation efficiency (SFE) (low protostar-to-core mass ratio) of just a few percent (Ward-Thompson et al. 2007b), if these 'starless' cores did contain protostars *Spitzer* would detect them. Given the small number statistics here, it is therefore possible that sensitive mid-IR observations could uncover protostars associated with both cores 3 and 4, in which case six of the 22 cores would be associated with

protostars. (Note also that core 4 may be associated with the CO outflow W-CO-flow1.)

Hence, in L 1495, it seems reasonable to assume that we have 5 ± 1 protostellar cores and 17 ± 1 starless or pre-stellar cores; the ratio of cores that are associated with young stars to those that are not is in the range of 0.2–0.4. But how many of the starless cores are pre-stellar? OMK02, and Mizuno et al. (1994) before them, suggest that the fraction of $H^{13}CO^+$ cores in L 1495 that exceed the Jeans mass, are gravitationally bound, are undergoing some form of collapse and therefore are pre-stellar in nature is probably high: note that the $H^{13}CO^+$ cores identified by OMK02 are compact (radius $\leq$0.1 pc) and of high density ($\geq 10^5$ cm^{-3}, the critical density for excitation of the $H^{13}CO^+$ line used in their study). They find that 13 of the 22 cores (60 per cent) in L 1495 have an $H^{13}CO^+$ column density mass that exceeds the virial mass (these 13 include cores 3, 4, 13a, 13b and 16, i.e. five of the six candidate pre-stellar cores). This leads us to believe that nine of the 22 are neither pre-stellar nor protostellar, so we identify these as being starless. The ratio of pre-stellar to protostellar cores in L 1495 is therefore in the range $\sim$1.3–2.3, while the ratio of starless to pre-stellar cores is in the range of $\sim$1–1.3.

Although based on modest statistics, *the above arguments indicate that the pre-stellar phase is about as long lived as the protostellar phase, and that in L 1495 there are as many pre-stellar cores as starless cores.* Similar results have been found in Perseus (Hatchell et al. 2007a; Jørgensen et al. 2007; Davis et al. 2008; Hatchell & Fuller 2008) and in other low-mass star-forming regions (Visser, Richer & Chandler 2002; Enoch et al. 2007; Evans et al. 2009).

Evans et al. (2009) find the Class 0 lifetime to be $\sim 10^5$ yr and the Class 0 and I lifetimes combined to be about 5×10^5 yr. It is worth mentioning that these timescales are more or less consistent with the range in dynamical ages, 10^4–10^5 yr, measured for molecular outflows (Arce et al. 2007, and references therein); this is to be expected, given the statistical evidence that most protostars, particularly those associated with cores, drive molecular outflows (Davis et al. 2009).

Evans et al. (2009) also find the pre-stellar core lifetime to be of the order of 5×10^5 yr. OMK02, from their analysis of the data discussed here, estimate a very similar time-scale ($\sim 4 \times 10^5$ yr) for starless condensations in Taurus. If we assume a value of 5×10^5 yr for the protostellar lifetime of our sources, then we arrive at a pre-stellar lifetime of $\sim 9(\pm 3) \times 10^5$ yr. This is slightly longer than the time-scale found by Evans et al., although it is still consistent to within the combined errors. Furthermore, we find the lifetime of starless cores that are not gravitationally bound to also be of the order of 10^6 yr.

4.2 The relationship between cores and outflows

OMK02 estimate various parameters for the $H^{13}CO^+$ condensations in Taurus, including size, density and mass. We plot a number of these in Fig. 14: in Fig. 14(a), we chart core mass based on the integrated intensity in $H^{13}CO^+$ emission against core radius (see OMK02 for details); a plot using the core virial mass, also calculated by OMK02, looks very similar to this figure. In Fig. 14(b), we plot the $H^{13}CO^+$ line width against $H^{13}CO^+$ peak antenna temperature; both have been measured by OMK02 at the peak position in each of their $H^{13}CO^+$ cores. Cores associated with embedded stars and outflows or HH jets are identified in both figures with green diamonds and open blue squares, respectively.

The plots in Figs 14(a) and (b) suggest that the protostellar, outflow-driving cores are generally less massive, more compact and more quiescent than many of the observed condensations (although clearly not all of the compact $H^{13}CO^+$ cores are associated with outflows). At first glance, this seems to run against expectation, since other studies have found that higher mass cores are more likely to be pre-stellar (e.g. Jørgensen et al. 2007; Hatchell & Fuller 2008). However, one should note that the more massive $H^{13}CO^+$ cores are often larger (Fig. 14a) and less dense than their less massive counterparts; these objects may in fact harbour multiple, unresolved cores. Alternatively, these massive $H^{13}CO^+$ condensations may be younger than the protostellar cores, or may simply be gravitationally unbound and therefore not pre-stellar in nature.

For the $H^{13}CO^+$ cores that *are* associated with outflows and protostars, we find no correlation between core mass and outflow mass or kinetic energy (plots not shown). If anything, the more massive cores (4 and 16b) seem to be associated with the least massive flows. However, this comparison does not take into account the size of each core; Figs 14(c) and (d) indicate a possible correlation between core *density* and outflow mass, and an inverse correlation between core *size* and outflow mass, albeit for a very small number of cores and outflows. The implication here is that the build-up of outflow mass increases as the protostellar core contracts. This idea clearly requires further investigation, both observationally and theoretically. Even so, our results are consistent with the early analysis of the $H^{13}CO^+$ data by Mizuno et al. (1994), who find that condensations with embedded stars in Taurus tend to be smaller in size, more dense and less extended than those without. Similar results were found in the submm continuum survey of Ward-Thompson et al. (1994).

Finally, we have conducted a statistical analysis of the data plotted in Fig. 14 (Isobe et al. 1990). This suggests that there is a 93 per cent chance that the correlation between core mass and core radius is significant (i.e. there is a 7 per cent chance that the sample is random), for cores with stars and for cores with outflows; for the entire sample there is a much higher chance (>99 per cent) that the correlation is real, in part because of the much larger number of data points. Likewise, we find a >99 per cent chance that for all cores the line intensity is related to the line width (Fig. 14b), although when only cores with stars or cores with outflows are considered the distribution of points is far less likely to be real ($\sim$65 and <50 per cent, respectively). There is a 98.5 per cent chance that the linear relationship between outflow mass and core density in Figs 14(c) is real, though a reduced likelihood (85 per cent) that the distribution between outflow mass and core mass in Fig. 14(d) is significant. Strictly speaking, only the linear distribution of points in Fig. 14(c) is potentially real, although clearly both plots would benefit from additional data.

4.3 Star formation efficiency in L 1495 based on outflow statistics

In their study of the outflow activity in Perseus-West, Davis et al. (2008) note that the more massive clouds are associated with a greater number of outflows. They use cloud masses derived from extinction mapping by Kirk, Johnstone & Di Francesco (2006), who note that this is arguably the best way of tracing the diffuse atomic and molecular gas ($A_v \sim$ 3–7) in large molecular clouds. Kirk et al. also stress that only $\sim$5 per cent of the cloud mass resides in regions with H_2 column densities $>5 \times 10^{21}$ cm^{-3} ($A_v > 2.5$): in other words, only 5 per cent of the gas mass is locked in the starless and protostellar cores mapped in $H^{13}CO^+$ and in submm dust continuum emission with, e.g. SCUBA or SCUBA-2. Based on these measurements, in Perseus-West Davis et al. estimate that there is one outflow for every 44–88 $M_\odot$ of ambient material.

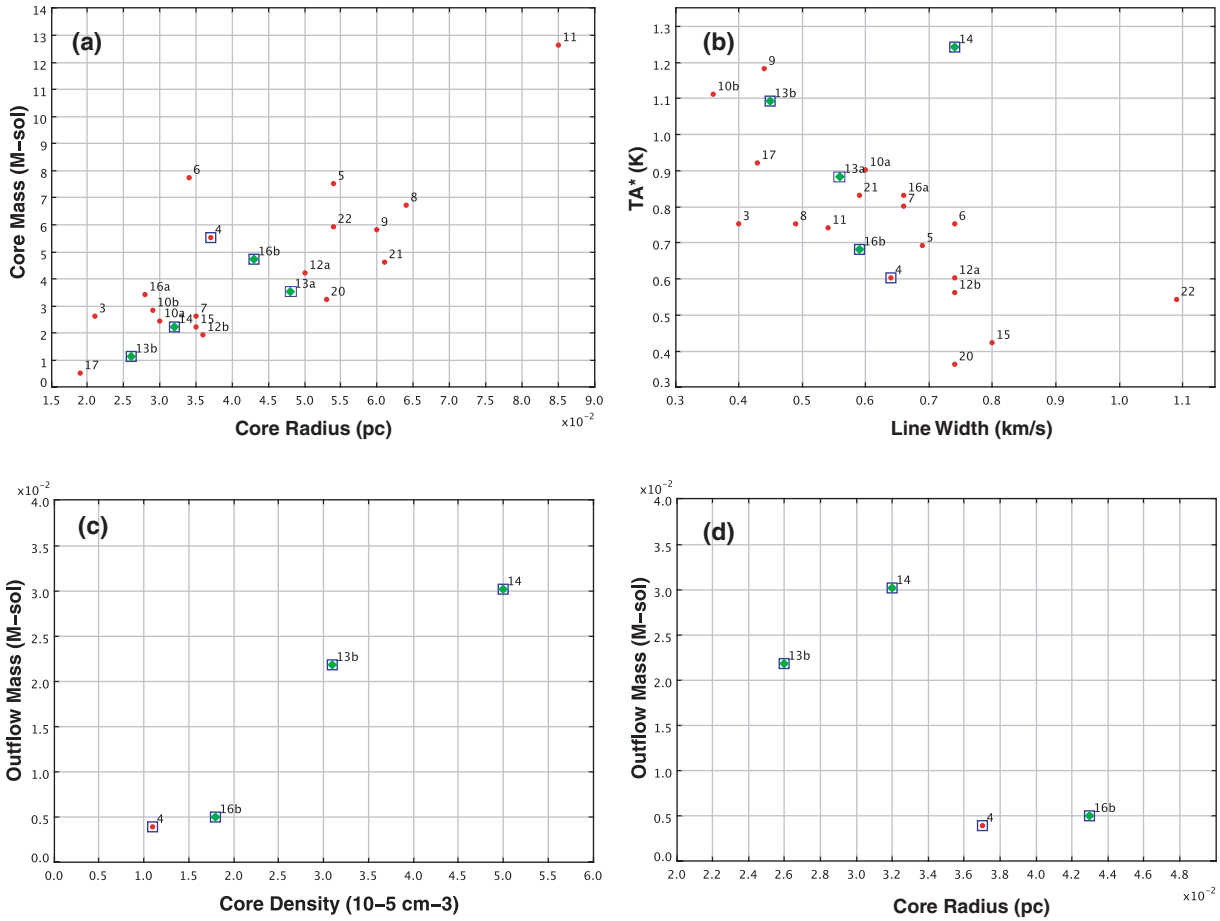

Figure 14. (a) Plot of $H^{13}CO^+$ core mass against core radius; (b) plot of $H^{13}CO^+$ line width against line intensity measured towards the peak in each core; (c) and (d) $H^{13}CO^+$ core molecular gas density and core radius plotted against the mass of the associated outflow. All core parameters are taken from table 2 of OMK02. In each panel, cores are marked with red dots and are labelled according to OMK02; cores associated with YSOs are marked with green diamonds; cores associated with molecular outflows or HH jets are marked with open blue squares (note that we were unable to measure the molecular flow mass for core 13a).

This range is not inconsistent with a canonical value for the SFE (SFE $= M_{\rm YSO}/[M_{\rm YSO} + M_{\rm core}]$) of ∼10-15 per cent (e.g. Jørgensen et al. 2007), if the cloud-to-core mass ratio is indeed ∼20, and the protostars have masses of the order of ∼0.5 $M_\odot$.

From their large-scale CO 2–1 and ^{13}CO 2–1 observations of Taurus, Goldsmith et al. (2008) find that the L 1495 bowl and SE ridge (regions they label L 1495 and B 213) have masses of the order of 2.6×10^3 and 1.1×10^3 $M_\odot$, respectively. Their observations are sensitive to H_2 column densities in excess of $\sim 1 \times 10^{21}$ cm^{-3} ($A_v > 0.5$), so somewhat similar to the columns of molecular gas probed by the extinction mapping technique used in Perseus. In L 1495, we list (in Table 2) nine outflows in the bowl and 12 in the L 1495 ridge; we therefore estimate roughly one outflow per 289 $M_\odot$ in the bowl, and one per 92 $M_\odot$ of gas in the ridge. These values are somewhat higher than in Perseus, especially in the bowl region. This is likely due to the more evolved state of this region, where the number of outflows underestimates the number of young stars and therefore the SFE. In the L 1495 bowl, a high percentage of young stars will be weak line TTSs that are no longer associated with molecular or even HH flows. Note also that Taurus in general is considered to be a less active region of star formation, being associated with less luminous young stars, narrower molecular line widths and lower kinetic temperatures than e.g. Perseus or Orion (Jijina, Myers & Adams 1999).

4.4 Outflows, cloud structure and the large-scale B-field in L 1495

Taurus has been the subject of many studies of the large-scale cloud structure and its relationship to the surrounding magnetic field; Heyer (1988) and Goodman et al. (1992) measure the polarization of background optical and IR starlight via selective dust absorption, observations which illustrate the field orientation in the outer, low column density regions. Troland et al. (1996) and Crutcher & Troland (2000) present complementary Zeeman effect observations in 18 cm OH emission. Although these probe higher column densities, they only yield information on the line-of-sight field component, and are of lower (arcminute) spatial resolution. To better trace the B-field that pervades the dense cores and high-density gas that envelopes these cores, one requires high spatial resolution observations of polarized submm continuum emission from magnetically aligned grains (e.g. Matthews, Wilson & Fiege 2001; Matthews, Fiege & Moriarty-Schieven 2002; Crutcher et al. 2004).

From studies of other low- and intermediate-mass star-forming regions we know that the field orientation, projected on to the plane of the sky, often snakes through filaments and cores, changing direction on tenths of parsec scales (e.g. Davis et al. 2000b; Momose et al. 2001; Houde et al. 2002; Matthews & Wilson 2002). Surveys of cores and clumps in star-forming clouds also reveal a general lack

of order in the orientations of the long axes of oblate starless and protostellar cores (e.g. Hatchell et al. 2005; Kirk et al. 2006); similarly, outflow surveys show that HH and H_2 line-emission jets are usually randomly orientated (Stanke, McCaughrean & Zinnecker 2002; Walawender et al. 2005; Davis et al. 2009). Together, these data suggest that the magnetic field in the *high-density regions* is poorly coupled to the neutrals, allowing ambipolar diffusion to build up mass on star-forming cores, or that the magnetic energy is insufficient to overcome the kinetic energy associated with the dense clumps and cores. Either way, the orientation of outflows and their associated protostellar cores do not appear to be strongly linked to the large-scale B-field.

But could L 1495 be an exception to the rule? The SE ridge in L 1495 is notable for being orientated roughly perpendicular to the surrounding B-field (Goodman et al. 1992; Heiles 2000; Goldsmith et al. 2008). Goodman et al. give a mean polarization position angle along the ridge of 27° from optical data, and 31° from IR polarization measurements. Goldsmith et al. (2008) overplot polarization vectors (compiled by Heiles 2000) on to their ^{13}CO integrated intensity map of Taurus and find that the field is not only perpendicular to the L 1495 ridge, but is aligned with 'striations' in the surrounding low column density medium. This suggests that – in these *low-density* regions – the B-field is well coupled to the molecular gas through ion-neutral collisions (UV penetration maintaining a degree of ionization in the gas). Collapse along these field lines may then produce the chain of high-density condensations that forms the SE ridge in L 1495. Although the field within the dense ridge awaits sensitive submm continuum polarization measurements (these are planned as part of the GBS), we point out here that many of the outflows found along the SE ridge are orientated perpendicular to the ridge, and *parallel* with the field direction in the surrounding low column density gas. This observation is in general disagreement with the results of Greaves, Holland & Ward-Thompson (1997), who in a study of five protostars with outflows find that if the flow is in the plane of the sky, the field tends to be orientated *perpendicular* to the flow axis. However, Greaves et al. used submm continuum polarization measurements and therefore probed the higher column density regions close to each outflow source. It will be interesting to see whether the field direction, measured with the polarimetry facility currently being developed for SCUBA-2, changes close to the young outflow sources in L 1495.

5 CONCLUSIONS

HARP observations in CO 3–2 emission are shown to be ideal for tracing outflow activity in nearby star-forming regions. The observations discussed here reveal as many as 16 molecular outflows in L 1495; most are associated with HH objects and/or molecular hydrogen line-emission features (MHOs). Candidate outflow driving sources (protostars or TTSs) are identified for eight CO flows, although only four of these flow progenitors appear to be associated with $H^{13}CO^+$ cores. Even so, we note that the CO outflow-driving sources have redder near-IR colours than their HH jet-driving counterparts. We also find a possible correlation between outflow mass and the associated core density and size, the more massive flows being associated with the denser, more compact cores.

OMK02 find that 13 of the 22 $H^{13}CO^+$ cores in L 1495 have a column density mass that exceeds the virial mass. Of these 13 cores, five seem to be associated with protostars (and four of these drive outflows). We estimate that the ratio of pre-stellar to protostellar cores in L 1495 is approximately in the range 1.3–2.3; the ratio of starless to pre-stellar cores is estimated to be ∼1.

Overall, we find that the bowl is more evolved than the SE ridge in L 1495; in the bowl there is a paucity of molecular outflows though a larger fraction of TTSs. The fact that the ridge is spatially more compact (long and narrow) in comparison to the bowl supports this interpretation. The SFE in L 1495 (particularly the SE ridge), estimated from the ambient cloud density, a canonical value for the cloud-to-core mass ratio, and the observed number of outflows, is consistent with other low-mass star-forming regions.

In comparison to Orion and Perseus, there is a modest number of outflows and protostars in L 1495. However, the region, especially the SE ridge, is relatively simple (in comparison to, say, NGC 1333), with little chance for source confusion and outflows overlapping other outflows or unrelated molecular cores. The statistics, though modest, are therefore likely to be more robust than in other regions.

ACKNOWLEDGMENTS

We thank the anonymous referee for his/her comments, which improved the overall quality of this paper. The James Clerk Maxwell Telescope is operated by the Joint Astronomy Centre (JAC) on behalf of the Science and Technology Facilities Council (STFC) of the United Kingdom, the Netherlands Organisation for Scientific Research and the National Research Council of Canada. UKIRT is operated by the JAC on behalf of the STFC. We acknowledge the Cambridge Astronomical Survey Unit (CASU) and the WFCAM Science Archive (WSA) for the processing and distribution of the near-IR data presented in this paper. This research used the facilities of the Canadian Astronomy Data Centre operated by the National Research Council of Canada with the support of the Canadian Space Agency.

REFERENCES

Arce H. E., Sargent A. I., 2006, ApJ, 646, 1070
Arce H., Shepherd D., Gueth F., Lee C. F., Bachiller R., Rosen A., Beuther H., 2007, in Reipurth B., ed., Protostars and Planets V. Univ. Arizona Press, Tucson, p. 245
Bourke T. L. et al., 2006, ApJ, 649, L37
Buckle J. V. et al., 2009, MNRAS, 399, 1026
Buckle J. V. et al., 2010, MNRAS, 401, 204
Bussmann R. S., Wong T. W., Hedden A. S., Kulesa C. A., Walker C. K., 2007, ApJ, 657, L33
Cabrit S., Bertout C., 1990, ApJ, 349, 530
Cavanagh B., Jenness T., Economou F., Currie M. J., 2008, Astron. Nachr., 329, 295
Crapsi A. et al., 2005, A&A, 439, 1023
Crutcher R. M., Troland T. H., 2000, ApJ, 537, L139
Crutcher R. M., Nutter D., Ward-Thompson D., Kirk J. M., 2004, ApJ, 600, 279
Curtis E. I., Richer J. S., Buckle J. V., 2010, MNRAS, 401, 455
Davis C. J., Smith M. D., Moriarty-Schieven G. H., 1998, MNRAS, 387, 954
Davis C. J., Dent W. R. F., Matthews H. E., Coulson I. M., McCaughrean M. J., 2000a, MNRAS, 318, 952
Davis C. J., Chrysostomou A., Matthews H. E., Jenness T., Ray T. P., 2000b, ApJ, 530, L115
Davis C. J., Scholz P., Lucas P. W., Adamson A., 2008, MNRAS, 387, 954
Davis C. J. et al., 2009, A&A, 496, 153
Davis C. J., Gell R., Khanzadyan T., Smith M. D., Jenness T., 2010, A&A, 511, A24
Di Francesco J., Evans N. J. II, Caselli P., Myers P. C., Shirley Y., Aikawa Y., Tafalla M., 2007, in Reipurth B., ed., Protostars and Planets V. Univ. Arizona Press, Tucson, p.17

Di Francesco J., Johnstone D., Kirk H., MacKenzie T., Ledwosinska E., 2008, ApJS, 175, 277
Dobashi K., Uehara H., Kandori R., Sakurai T., Kaiden M., Umemoto T., Sato F., 2005, PASJ, 57, 1
Eislöffel J., Mundt R., 1998, AJ, 115, 155
Elias J. H., 1978, ApJ, 224, 857
Enoch M. L., Glenn J., Evans N. J., Sargent A. I., Young K. E., Huard T. L., 2007, ApJ, 666, 982
Evans N. J. et al., 2009, ApJS, 181, 321
Frerking M. A., Langer W. D., Wilson R. W., 1982, ApJ, 262, 590
Giannini T., Nisini B, Lorenzetti D., 2001, ApJ, 555, 40
Goldsmith P. F., Heyer M. H., Narayanan G., Snell R., Li D., Brunt C., 2008, ApJ, 680, 428
Gomez M., Whitney B. A., Kenyon S. J., 1997, AJ 114, 1138
Gómez de Castro A. I., 1993, ApJ, 412, L43
Goodman A. A., Jones T. J., Lada E. A., Myers P. C., 1992, ApJ, 399, 108
Gottlieb D. M., Upson W. L., 1969, ApJ, 157, 611
Graves S. F. et al., 2010, MNRAS, submitted
Greaves J. S., Holland W. S., Ward-Thompson D., 1997, ApJ, 480, 255
Hartmann L., Megeath S. T., Allen L., Luhman K., Calvet N., D'Alessio P., Franco-Hernandez R., Fazio G., 2005, ApJ, 629, 881
Hatchell J., Dunham M. M., 2009, A&A, 502, 139
Hatchell J., Fuller G. A., 2008, A&A, 482, 855
Hatchell J., Fuller G. A., Ladd E. F., 1999, A&A, 346, 584
Hatchell J., Richer J. S., Fuller G. A., Qualtrough C. J., Ladd E. F., Chandler C. J., 2005, A&A, 440, 151
Hatchell J., Fuller G. A., Richer J. S., 2007a, A&A, 472, 187
Hatchell J., Fuller G. A., Richer J. S., Harries T., Ladd E. F., 2007b, A&A, 468, 1009
Heiles C., 2000, AJ, 119, 923
Heyer M. H., 1988, ApJ, 324, 311
Holland W. S. et al., 2006, in Zmuidzas J., Holland W. S., Withington S., Duncan W. D., eds, Proc. SPIE Vol. 6275, SCUBA-2: a 10 000-Pixel Submillimeter Camera for the James Clerk Maxwell Telescope. SPIE, Bellingham, p. 45
Houde M. et al., 2002, ApJ, 569, 803
Hovey G. J. et al., 2000, in Butcher H. R., ed., Proc. SPIE Vol. 4015, Radio Telescopes. SPIE, Bellingham, p. 114
Isobe T., Feigelson E. D., Akritas M. G., Babu G. J., 1990, ApJ, 364, 104
Jenness T., Cavanagh B., Economou F., Berry D. S., 2008, in Argyle R., Bunclark P. S., Lewis J. R., eds, ASP Conf. Ser. Vol. 394, Data Analysis Software Systems. Astron. Soc. Pac., San Francisco, p. 565
Jijina J., Myers P. C., Adams F. C., 1999, ApJS, 125, 161
Jørgensen J. K. et al., 2006, ApJ, 645, 1246
Jørgensen J. K., Johnstone D., Kirk H., Myers P. C., 2007, ApJ, 656, 293
Jørgensen J. K., Johnstone D., Kirk H., Myers P. C., Allen L. E., Shirley Y. L., 2008, ApJ, 683, 822
Kenyon S. J., Hartmann L., 1995, ApJS, 101, 117
Kenyon S. J., Gómez M., Whitney B. A., 2009, in Reipurth B., ed., Handbook of Star Forming Regions, Vol. 1. ASP monographs. Astron. Soc. Pac., San Francisco, p. 405
Kirk H., Johnstone D., Di Francesco J., 2006, ApJ, 646, 1009
Knee L. B. G., Sandell G., 2000, A&A, 361, 671
Koornneef J., 1983, A&A, 128, 84
Langer W. D., Wilson R. W., Goldsmith P. F., Beichman C. A., 1989, ApJ, 337, 355
Lawrence A. et al., 2007, MNRAS, 379, 1599
Lee C.-F., Mundy L. G., Stone J. M., Ostriker E. C., 2002, ApJ, 576, 294
Lee C.-F., Ho P. T. P., Palau A., Hirano N., Bourke T. L., Shang H., Zhang Q., 2007, ApJ, 670, 1188
Lucas P. W. et al., 2008, MNRAS, 391, 136
Luhman K. L., Whitney B. A., Meade M. R., Babler B. L., Indebetouw R., Bracker S., Churchwell E. B., 2006, ApJ, 647, 1180
McCuskey S. W., 1939, ApJ, 89, 568
McGroarty F., Ray T. P., 2004, A&A, 420, 975
Matthews B. C., Wilson C. D., 2002, ApJ, 574, 822
Matthews B. C., Wilson C. D., Fiege J. D., 2001, ApJ, 562, 400
Matthews B. C., Fiege J. D., Moriarty-Schieven G. H., 2002, ApJ, 569, 304
Matthews H. E., McCutcheon W. H., Kirk H., White G. J., Cohen M., 2008, AJ, 136, 2083
Meyer M. R., Calvet N., Hillenbrand L. A., 1997, AJ, 109, 1682
Mizuno A., Onishi T., Hayashi M., Ohashi N., Sunada K., Hasegawa T., Fukui Y., 1994, Nat, 368, 719
Mizuno A., Onishi T., Yonekura Y., Nagahama T., Ogawa H., Fukui Y., 1995, ApJ, 445, L16
Momose M., Tamura M., Kameya O., Greaves J. S., Chrysostomou A., Hough J. H., Morino J. I., 2001, ApJ, 555, 855
Motte F., André P., 2001, A&A, 365, 440
Narayanan G., Heyer M. H., Brunt C., Goldsmith P. F., Snell R., Li D., 2008, ApJS, 177, 341
Onishi T., Mizuno A., Kawamura A., Ogawa H., Fukui Y., 1996, ApJ, 465, 815
Onishi T., Mizuno A., Kawamura A., Tachihara K., Fukui Y., 2002, ApJ, 575, 950 (OMK02)
Pineda J. E., Caselli P., Goodman A. A., 2008, ApJ, 679, 481
Racine R., 1968, AJ, 73, 233
Rieke G. H., Lebofsky M. J., 1985, ApJ, 288, 618
Santiago-García J., Tafalla M., Johnstone D., Bachiller R., 2009, A&A, 495, 169
Smith H. et al., 2003, in Phillips T. G., Zmuidzinas J., eds, Proc. SPIE Vol. 4855, Millimeter and Submillimeter Detectors for Astronomy. SPIE, Bellingham, p. 338
Stanke T., Williams J. P., 2007, AJ, 133, 1307
Stanke T., McCaughrean M. J., Zinnecker H., 2002, A&A, 392, 239
Strom K. M., Strom S. E., 1994, ApJ, 424, 237
Tafalla M., Myers P. C., Caselli P., Walmsley C. M., Comito C., 2002, ApJ, 569, 815
Tafalla M., Santiago J., Johnstone D., Bachiller R., 2004, A&A, 423, L21
Tatematsu K., Umemoto T., Kandori R., Sekimoto Y., 2004, ApJ, 606, 333
Torra J., Fernández D., Figueras F., 2000, A&A, 359, 82
Torres R. M., Loinard L., Mioduszewski A. J., Rodríguez L. F., 2009, ApJ, 698, 242
Troland T. H., Crutcher R. M., Goodman A. A., Heiles C., Kazes I., Myers P. C., 1996, ApJ, 471, 302
Ungerechts H., Thaddeus P., 1987, ApJS, 63, 645
van Kempen T. A. et al., 2009, A&A, 501, 633
Visser A. E., Richer J. S., Chandler C. J., 2002, AJ, 124, 2756
Walawender J., Bally J., Kirk H., Johnstone D., 2005, AJ, 130, 1795
Ward-Thompson D., Scott P. F., Hills R. E., André P., 1994, MNRAS, 268, 276
Ward-Thompson D. et al., 2007a, PASP, 119, 855
Ward-Thompson D., André P., Crutcher R., Johnstone D., Onishi T., Wilson C., 2007b, in Reipurth B., ed., Protostars and Planets V. Univ. Arizona Press, Tucson, p. 33
Williams J. P., Plambeck R. L., Heyer M. H., 2003, ApJ, 591, 1025
Wilson T. L., 1999, Rep. Prog. Phys., 62, 143
Yeh S. C. C., Hirano N., Bourke T. L., Ho P. T. P., Lee C-.F., Ohashi N., Takakuwa S., 2008, ApJ, 675, 454

This paper has been typeset from a TEX/LATEX file prepared by the author.